2up

The Characteristics of a Possible Low Altitude

Electron Layer in the Martian Atmosphere

By

Herbert Andrew Wallio

B.S. June 1965, Virginia Polytechnic Institute

A Thesis submitted to

The Faculty of

The School of Engineering and Applied Science
of The George Washington University in partial satisfaction
of the requirements for the degree of Master of Science

December 1973

Thesis directed by

Henry G. Reichle, Jr.

TABLE OF CONTENTS

ABSTRACT

The apparent diurnal Martian surface pressure variation, as deduced from radio occultation experiments, is discussed and explained as possibly arising from the effect of a low altitude electron layer. Possible source and loss mechanisms for the low altitude electron layer are presented and discussed. Time-dependent differential equations describing the electron layer are derived and then integrated to investigate the electron distribution resulting from the several processes that might occur in the atmosphere. It is concluded that the source mechanism is the sublimation of alkali atoms from a permanent dust layer (a dust layer of 0.2 micron particles of density 9 cm^{-3} is sufficient), and that the dominant loss process must involve CO_2 clustering to the alkali atoms. Using these processes, an electron layer is developed which would explain the apparent diurnal surface pressure.

LIST OF TABLES

LIST OF FIGURES

LIST OF SYMBOLS

A	coefficient used to define alkali height distribution
A	symbol for as yet unidentified alkali atom
B	coefficient used to define alkali height distribution
e^-	symbol for electron and charge on electron
f	dynamical flattening coefficient (Chapter III)
f	frequency of radio wave
g	acceleration due to gravity (Mars)
H	scale height in atmosphere
h	altitude along ionization path
I	intensity of sunlight along ionization path
I_0	intensity of sunlight outside atmosphere
$\vec{J}$	electron current vector
K	constant used to define alkali number density
K_{mn}	rate coefficient for reaction mn
L	a term which accounts for the loss of electrons
m	mass of electron
M	third particle (probably dust)
N	refractivity $\equiv (\mu - 1) \times 10^6$
N_c	composite refractivity in the atmosphere
N_e	component of refractivity due to electrons
N_n	component of refractivity due to neutral particles
n_A	density of alkali atoms
n_{CO_2}	density of CO_2 molecules

n_n density of neutral molecules

p impact parameter (defined in Figure 5)

p_r probability of ionization

P a term which accounts for the electron production

P_o base surface pressure

P_1 measured surface pressure

Q absorption coefficient

R gas constant

R radius of planet

R a defined variable in Equation 9-2

S length along ionization path

T atmospheric gas kinetic temperature

t time

$\vec{V}$ transport velocity (Chapter VIII)

$\vec{V}$ electron velocity due to electric field (Appendix A)

X dummy variable

z altitude in atmosphere

α electron recombination coefficient

Δ number of electrons released per captured photon

ε_c dielectric constant of composite atmosphere

ε_n dielectric constant of neutral atmosphere

ε_o dielectric constant of free space

λ wavelength of light

σ cross section of CO_2 absorption

σ conductivity of the electron gas

ω angular frequency of radio ray

Subscripts

A   refers to alkali atoms

c   refers to composite atmosphere

e   refers to electrons

i   refers to an ith measurement

n   refers to the neutral atmosphere

o   refers to a base level

CHAPTER I. Introduction

Since 1965, there have been four U.S. planetary space probes used in the exploration of the planet Mars. These spacecraft were used to gather data concerning the physical properties of the planet, and one of the primary areas of research was the determination of the physical properties of the Martian atmosphere. These properties were examined by techniques of visual imagery (refs. 1,2,3), infrared spectroscopy (refs. 4,5,6), infrared radiometry (refs. 7,8) ultraviolet spectrometry (refs. 9,10,11,12), and radio occultation (refs. 13,14,15,16,17, 18,19).

Analyses of radio occultation data from the U.S. Mariner spacecraft have produced a considerable amount of information on both the neutral atmosphere and ionosphere of Mars. Data from a single occultation entry and exit were obtained from each of the flyby missions of Mariners 4 (1965), 6 and 7 (1969), and data from a large number of occultations of the Mariner 9 (1971) orbiter have greatly extended the latitudinal, longitudinal, and diurnal coverage of the planet.

On the basis of the currently available analysis of the Mariner radio occultation data (refs. 16,17), there are some indications of apparently systematically higher surface pressures on the nightside of Mars than on the dayside. This difference is approximately 1 mb or roughly 20 percent of the total pressure. These indications of an apparent diurnal variation in surface pressure might be explained by either a variation in topography at the occultation location, or by some sort of diurnal process occurring in the atmosphere. This paper

will discuss one atmospheric diurnal process that might explain the radio occultation results.

In a radio occultation experiment, as the spacecraft passes behind the planet the atmosphere acts as a lens to the radio ray and changes the apparent motion of the spacecraft. The changes in motion of the spacecraft are measured by the change in frequency of the received radio ray (Doppler signal). After subtracting the predicted change in spacecraft motion from the measured Doppler change, the difference or residual is used to deduce the atmospheric density. It has been shown that there are interpretation ambiguities inherent in the reconstruction of atmospheric properties from single frequency radio occultation data (ref. 20). This ambiguity arises from the fact that the deduced refractivity can be composed of both a positive component (due to the neutral atmosphere which causes an apparent motion away from the observer) and a negative component (due to the presence of free electrons which cause an apparent motion towards the observer). Thus, a single frequency occultation measurement can be represented by one equation with two unknowns which cannot be solved for the effects of the two components separately. Because of this interpretation ambiguity, numerous atmospheric models (representing different atmospheric states) can be developed that will produce the refractivity profile obtained from any single frequency radio occultation experiment. One atmospheric model that accounts for the apparent pressure disparity includes a time-dependent low altitude electron layer in the dayside atmosphere (ref. 26).

The properties of a planetary atmosphere and ionosphere vary with altitude, latitude, longitude, and the local time of day. A low-altitude electron layer will possess similar variations. This paper will discuss an atmospheric model that includes an electron layer, and will develop equations to describe the altitude and time variations of the layer. To do this, the simplified (no transport) time-dependent electron density continuity equation is normalized and non-dimensionalized for ease of handling. The resulting first order, non-linear, differential equation is integrated to give diurnal electron density profiles as a function of various absorption and recombination coefficients. The development of these models is somewhat the reverse of that associated with the classical Chapman electron layer theory. In that theory, the atmospheric properties are known and the resulting electron layer is determined. In the present case, the magnitude and functional form of the electron layer at a specific geographic location and local time is specified by the difference between the refractivity resulting from the neutral atmosphere and the refractivity as measured by radio occultation. Knowing the electron distribution then allows the distribution of the ionizable constituent to be determined. The recombination and the absorbtion coefficients in the atmospheric model are empirically adjusted until an acceptable ionizing constituent model which produces the specified electron distribution results.

The next section of this paper will provide a brief description of the radio occultation experiment and the methods by which the physical properties of the Martian atmosphere are inferred from the occultation

experiments. Following that is a section that discusses the diurnal pressure variation as it appears in the existing data, and another section that describes the use of that variation to estimate the functional form of the proposed electron layer. There are then several sections that discuss the electron layer -- its description, origin, and methods for modeling it. The remainder of the paper summarizes the derivation of the equations used in the model, and presents the results of the numerical integration of those equations. On the basis of these results, conclusions concerning the electron layer and the inferred source distribution are drawn.

CHAPTER II. Radio Occultation and the Martian Atmosphere

The radio occultation occurs as a spacecraft passes behind a planet as viewed from the tracking station. The radio signal between the spacecraft and tracking station is changed by passing through the atmosphere of the planet being studied. By making certain assumptions about the atmosphere, the position of the spacecraft, the propagation paths, and the change in the received radio frequency (Doppler) as the radio ray passes through the atmosphere can be related to the index of refraction of the atmosphere. Since the index of refraction (μ) of most gases is numerically very close to unity, the quantity generally used in describing the atmosphere is the refractivity unit. The refractivity is related to the index of refraction as:

$$N \equiv (\mu - 1) \cdot 10^6 .$$

Figure 1 is a sketch of a typical profile of refractivity versus altitude for the atmosphere of Mars. Plots such as Figure 1 are the usual output of radio occultation experiments, and it is these plots that form the basis for the inference of atmospheric properties. The negative refractivity peak which occurs at 135 km on the dayside profile is attributed to free electrons resulting from photoionization processes involving CO_2 in the Martian atmosphere. If there are at most a very small number of low mass ions present (a reasonable assumption for the atmosphere of Mars), the number of free electrons is simply related to the negative refractivity by a linear equation.

The lower positive peak is assumed, by most authors, to be caused only by the neutral atmosphere. The relationship between the refractivity and the properties of the neutral atmosphere is more complex than that for electrons since there can be several gases which contribute to the refractivity and only one equation relating them. Therefore, the exact gas composition must either be known or assumed, and the refractivity profile is used to determine the molecular number density. The molecular number density is used together with the hydrostatic equation and the perfect gas law to arrive at the temperature distribution in the atmosphere. The pressure variation in the atmosphere can be obtained by either integrating the number density in the hydrostatic equation or by using the temperature distribution in the perfect gas law.

The peak dayside electron density, as deduced from the Mariner radio occultation, occurs at about 135 km with a magnitude of approximately 1.6×10^5 electrons per cm^3. The deduced surface temperatures vary from $141^{\circ}K$ to $272^{\circ}K$ with about $240^{\circ}K$ being the average dayside surface temperature and about $160^{\circ}K$ being the average nightside surface temperature. The deduced lapse rate in the atmosphere varies from 0 to + $3.8^{\circ}K/km$, with a large number of measurements implying a near isothermal atmosphere, and almost all measurements having a lapse rate of less than half the theoretical adiabatic lapse rate ($5^{\circ} K/km$) (ref. 19). (These small temperature gradients are the basis of using, in the following sections, the approximation that the atmosphere is isothermal very near the surface. The error in pressure using an isothermal

approximation over a height of 10 km will be no larger than about 3 percent at 10 km.) The deduced Martian surface pressures vary from 2.5 mb to 10.8 mb, with the average surface pressure being from 4.7 to 6.1 mb, depending on what surface is taken to be representative of the mean planet surface.

CHAPTER III.   Description of the Apparent Diurnal Variation in the

Surface Pressure

On the basis of the currently available analysis of the Mariner

radio occultation data (refs. 16,17,18), there are indications of ap-

parent systematically higher surface pressures on the nightside of

Mars than on the dayside. It is difficult to examine the published

occultation surface pressures as a group, since the data occurs at

different altitudes, places, times of day, and time of year. To com-

pare the data as a group, the effects of different altitudes and tem-

peratures in the atmosphere are taken into account, and any of the

previously mentioned effects (including season and meteorology) will be

assumed to cancel out when group averages are taken.

- A reasonable approximation for a Martian equipotential surface can

be obtained from the dynamical flattening (ref. 21). An approximation

to the equipotential radius as a function of latitude is $R \approx R_{eq}$ [1 -

$f \sin^2$ (LAT)], where R_{eq} is the equatorial radius, f the flattening co-

efficient, and LAT is the latitude of the point in question. From

Mariner 9 orbital analysis (refs. 22,23) the flattening coefficient,

f, was measured to be 5.25×10^{-3}, and this value will be used in the

following analysis.

To allow for the different values of deduced surface temperatures

and altitudes associated with each deduced surface pressure, the de-

duced surface pressures will be compared by two methods. The first

method is to scale each surface pressure data to a pressure altitude.

The pressure altitude is the altitude in a reference atmosphere at

which a given pressure level occurs. To illustrate this, assume that the Martian equipotential surface has the same dayside and nightside pressure (P_o) at the zero altitude or base surface, then for a deduced pressure, P_i, temperature, T_i (associated scale height, $H_i = \dfrac{RT_i}{mg}$), and altitude, Z_i,

$$P_i = P_o \exp \left\{ - \frac{Z_i}{H_i} \right\} .$$

The reference atmosphere is taken to have the same equipotential surface, the same zero altitude pressure, P_o, a constant temperature, T_o, (and, therefore, scale height, H_o) over the entire reference surface. Then, for the same deduced pressure, P_i, there is a pressure altitude, Z_{oi}, such that

$$P_i = P_o \exp \left\{ - \frac{Z_{oi}}{H_i} \right\} ,$$

and therefore, the pressure altitude associated with each P_i, T_i, and Z_i, deduced from a radio occultation experiment, is defined as

$$Z_{oi} = \frac{H_o}{H_i} Z_i .$$

Now, if the base surface pressure is the same for both the dayside and nightside surface, then the ln of the pressure data plotted against the pressure altitude should all lie on a straight line (within the measurement accuracy and the assumption of an isothermal

atmosphere over the heights in question).

Figure 2 is a plot of ln of pressure versus pressure altitude above a geopotential ($R_{equator}$ = 3390 km, f = 5.25 × 10^{-3}) for a set of night (exit) and day (entrance) deduced surface pressures. A reference temperature of 240°K was used and therefore H_o = 12 km and the deduced surface temperature at each data point was used for H_i to calculate the pressure altitude. As can be seen from Figure 2, the nightside (exit) pressure measurements cluster above the line through the dayside pressures, implying the assumption of an equal base surface pressure, for both the dayside and nightside, was invalid.

The second way to compare the data is to examine the base surface pressure P_o by the relation

$$P_o = P_i \exp \left\{ + \frac{Z_i}{H_i} \right\} ,$$

where P_i, Z_i, and H_i are the surface pressure, altitude from the geopotential, and surface temperature deduced from the radio occultation experiment. Figure 3 is a plot of the calculated base surface pressure versus relative time of day for a set of day (entry) and night (exit) measurements referenced to a geopotential. Again the difference between day and night pressure measurements is evident and is approximately 1 mb.

Since it is considered unlikely that a day-night pressure differential of such magnitude (20% of the total pressure) could actually be sustained for any appreciable time, some process or combination of

out that if there are free electrons below 50 km on the dayside, these electrons would contribute a negative component to the refractivity in this region. The observed refractivity would then be a composite of the negative refractivity due to the free electrons and the positive refractivity due to the neutral atmosphere. The observed composite refractivity would then be smaller than that of the actual neutral component of refractivity, and therefore, the pressure deduced from the observed refractivity would be less than the actual atmospheric pressure.

CHAPTER IV. Estimation of the Form of the Electron Layer

If it is assumed that the dayside positive portion of the lower refractivity profile, as shown in Figure 3, is a composite profile of the neutral atmosphere plus an electron layer, then it can be shown that real part of the index of refraction is (see Appendix A):

$$\mu_c^2 = \mu_n^2 - n\,(e^-)^2\left[(4\pi)^2 \epsilon_o m\, f^2\right]^{-1} \qquad \text{4-(1)}$$

where μ_c is the measured composite real index of refraction, μ_n is the real index of refraction of the neutral atmosphere, and the remaining terms are the contribution of the electron layer (where n is the number of electrons, e^- and m are the charge and mass of an electron, ϵ_o is the dielectric constant of free space, and f is the frequency of the probing radio signal).

Rearranging Equation (1) and introducing refractivity $N \equiv (\mu - 1) \times 10^6$

$$N_e = -1 + \left[1 - (1+N_n)^2 + (1+N_c)^2\right]^{1/2} \qquad \text{4-(2)}$$

where N_e is the refractivity of the electron distribution, N_c is the measured refractivity, and N_n is the refractivity of the neutral atmosphere. Equation (2) can be approximated to: (see Appendix A)

$$\text{4-(3)}$$

$$N_e \approx N_c - N_n$$

Assuming that the atmosphere is in hydrostatic equilibrium and that the neutral refractivity is proportional to the neutral density (a valid assumption for the low gas density on Mars), then

$$N_n(z) = N_n(0) \exp\left\{- z/H_n\right\}$$

4-(4)

where Z is the altitude above the geopotential and H_n is the scale height of the neutral atmosphere

$$H_n \equiv Z \left\{ \int_0^z \frac{mg}{RT} dz \right\}^{-1}$$

4-(5)

By assuming that the deduced nightside surface pressure is more indicative of the actual surface pressure, and by allowing various formulations for H_n, i.e., isothermal, constant temperature gradients, etc., many models of electron distributions can be derived. Figure 4 is a sketch of electron number density versus altitude for several derived electron distribution models. The upper solid curve is the ionosphere electron layer that is deduced by radio occultation for most dayside occultations. The lower curves are the calculated electron distribution models which would essentially equalize the surface pressure, and would still yield the same refractivity profile as the refractivity profile observed by the radio occultation experiment. As can be seen from Figure 4, these calculated layers all have peak densities of 6 to 8 × 10^4 electrons per cm^3 and the peak density occurs at altitudes below 15 km. It should also be noted that the calculated

electron density profiles are only rough estimates, since the data
from which they are calculated consist primarily of published numbers
of the pressure at the point of radio occultation and the measured re-
fractivity profiles in the atmosphere (of which very few have been
published). To compound the problem there are large differences in
the surface pressures, deduced from the same radio occultation data,
by different authors. "The difference . . . is due to the method of
removing from the Doppler residuals, drifts, and oscillation, whose
presence is not understood by the Mariner experimenters." (See refer-
ence 27.)

CHAPTER V. Source of the Proposed Electron Layer

In the past, Martian ionospheric models have been extremely controversial, and a considerable amount of research has been done on the upper ionosphere of Mars (refs. 13,28,29,30,31). Although the existence of low electron layers on Mars has been conjectured (ref. 31) and electron density of the order of $10^4 cm^{-3}$ peaked at 65 km have been measured (ref. 32), little research has been reported on the lower ionosphere. Whitten, et al. (refs. 33,34) have studied the lower Martian ionosphere by studying the influx of solar protons and cosmic rays on a CO_2 atmosphere. They concluded that for a quiet sun the lower ionosphere below 65 km is formed predominately by galactic cosmic rays, and is a permanent layer with little diurnal variation peaked at approximately 25 to 35 km with a maximum density of the order of 10^3 electrons cm^{-3}.

Since all of the efficient channels of electron production involving photochemical processes in gaseous carbon dioxide in the Martian atmosphere have been utilized in theoretical modeling of the ionosphere, the postulated electron layer must come from some additional process in the atmosphere. Also, since the effect of the electron layer is diurnal, the electron density should exhibit a diurnal variation. Assuming that this diurnal variation is driven by sunlight the source must be able to liberate electrons when exposed to solar ultraviolet radiation. It is known that CO_2 gas absorbs significantly in the 100 - 1700A° region (ref. 35) and CO_2 gas is completely transparent from about 1750A° to at least 2100A° (ref. 36).

The Martian atmosphere has very little ozone and therefore there is an ultraviolet window in the $1750A^{\circ}$ to $2100A^{\circ}$ region (ref. 35). Hence, light in this wavelength interval can reach the Martian surface. It follows then that the electron source material must release electrons when exposed to light in the $1800A^{\circ}$ to $2100A^{\circ}$ region (6.9 ev to 5.9 ev). Based on ionization potentials and abundance criteria, the list of source candidates has been reduced to: potassium (ionization potential = 4.3 eV), sodium (5.12 eV), barium (5.19 eV), lithium (5.36 eV), aluminum (5.96 eV), and calcium (6.09 eV). All of these materials are cosmically abundant and found in both planetary crustal material and meteoric dust.

This electron source material, alkali metals in the atmosphere, must come from either the top of the atmosphere (meteoric ablation), the bottom of the atmosphere (crustal material raised into the atmosphere by the wind), or a combination of the two methods. It is proposed that the alkali metals sublimate from aerosols or "dust" particles that have arrived in the atmosphere by one of the methods just mentioned.

CHAPTER VI. Dust and Aerosols in the Martian Atmosphere

Dust and aerosol particles in the Martian atmosphere have been observed and measured by many authors (refs. 37 thru 43). Thin detached haze layers were distinguished in Mariner photographs at altitudes of 5 to 45 km (ref. 44). The presence of dust in the atmosphere was found to be able to account for the fact that measured atmospheric temperatures were considerably warmer than the theoretical temperatures calculated, assuming radiative equilibrium in the atmosphere (ref. 45). The presence of a low altitude dust layer would also account for the observed photolytic stability of the Martian CO_2 atmosphere (ref. 46) and in addition this dust brings into agreement the observed and computed profiles of the minor constituents O, O_2, CO and O_3 (ref. 46). In fact some authors have concluded that there are aerosols, that absorb solar radiation, permanently present in the Martian atmosphere (ref. 47). This dust would most likely be composed of oxides of Si, Ti, Fe, Mn, Mg, Ca, and Na (ref. 48). The dust in the Martian atmosphere has a measured SiO_2 content of about 60 percent (ref. 39); and since this is a slightly enhanced silicon content, the alkaline content will also be enhanced (ref. 49). Therefore, if a .2µm particle lost 1/10,000 th of its weight in sublimated alkali atoms, it would release on the order of 2×10^4 alkali atoms into the atmosphere.

The dust could arrive in the atmosphere in either or both of two ways. First, the dust may be the result of the surface material having been broken up into fine powder by the extreme heating and cooling

differences experienced over a Martian day. This powdered surface material could easily be blown into the atmosphere by thermal winds (ref. 50,51) or localized dust storms which occur rather frequently (ref. 52). Since .2μ particles would remain in the atmosphere on the order of two years, it is concluded that the atmosphere may contain such particles most of the time (ref. 53). Second, the dust could result from the ablation of meteoroids which enter the atmosphere. This idea has been advanced as the source of sodium layers in the earth (ref. 54) and since Mars is closer to the asteroid belt than earth, the effect may be even more pronounced for Mars.

CHAPTER VII. Modeling of the Alkali Layer

Aerosol layers have been detected in the earth's lower atmosphere (refs. 55,56,57). Alkali metal layers have also been measured in the earth's atmosphere (refs. 54,58,59,60,61,62). The sodium layer in the earth's atmosphere has been postulated to come from an aerosol or "dust bank layer" (refs. 62,63,64), or from meteoric material (refs. 54,65, 66). The actual photochemical process and distributions in the earth's atmosphere are not too well understood or modeled, primarily because of the lack of quantitative atmospheric data, lack of laboratory measurements of the physical properties of metal ions and their oxides, and lack of knowledge as to the effects of competing reactions such as CO_2 clustering (ref. 67) and aerosol ion pair annihilation (ref. 68).

. It will be assumed that the final Martian alkali number distribution follows roughly the same shape as that found for earth's sodium distribution (such as shown in reference 65) and that this distribution can be adequately approximated by the equation:

$$n_A(z,0) = K \exp \left\{ -z/A - B e^{-z/A} \right\}$$

7-(1)

where $n_A(Z,0)$ is the alkali number density as a function of altitude (Z), at time, $t = 0$. A can be thought of as a "scale height" for the rate of fall of the upper side of the distribution and B is a dimensionless constant which controls the shape of the lower side of the distribution. As a starting basis, A was given the value of 6 km which is approximately one-half the neutral scale height as observed in

the earth's sodium layer (ref. 61). The altitude of peak density of the
alkali distribution is given by

$$Z_{(n_A max)} = A \ln B$$

Thus, the value of B was chosen to be 6 in order that the distribu-
tion peak occur at an altitude below 15 km (for the numbers chosen the
peak occurs at 10.75 km).

CHAPTER VIII.   Derivation of the Time-Dependent Electron Distribution

The continuity equation relates the change in electron density per unit time to the production, loss, and the divergence, and is given by:

$$\frac{\partial n_e}{\partial t} = P - L - \nabla \cdot (n_e \vec{v})$$

where N_e is the electron density, p is the production rate, L is the loss rate, and $\vec{V}$ is the transport velocity. It will be assumed that the transport terms can be neglected, so that the only terms to be derived are the production and loss rates. Figure 5 depicts the geometry and defines the variables used in the derivation. (As can be seen from Figure 5 the atmosphere is assumed to be spherically symmetric.) It is assumed that the absorbtion of ionizing solar radiation in an element of atmospheric pathlength, dS, is proportional to the radiation flux, I, the atmospheric alkali concentration, N_a, and the absorption cross section, Q, and thus can be written as

$$dI = -I Q n_a \, dS \qquad 8\text{-}(1)$$

where the I and Q are wavelength dependent. This wavelength dependence will be accounted for later in this development.

Now from Figure 5

$$\rho = (R + h)\sin\lambda = (R + Z)\sin\chi$$

and

$$S = -\rho \cot\lambda \qquad 8\text{-}(2)$$

where χ is the solar zenith angle, and so that $dS = pdsc^2\lambda d\lambda$ which will be used in Equation 8-(1).

In addition to loss of radiation due to ionization, there is a competing reaction from the absorption by CO_2 gas whose absorption coefficient is σ. Thus, Equation 8-(1) becomes

$$dI = -I\left(Qn_A + \sigma n_{CO_2}\right)dS \qquad \text{8-(3)}$$

It is assumed that the diurnal variation in the concentration of the alkali material is very small (in keeping with the long lifetime of the particles); and since their number density is also small, the removal of a source atom must be accounted for in some manner.

. Therefore, let

$$n_A(h,t) = n_A(h,o) - n_e(Z,t) \qquad \text{8-(4)}$$

Initial calculations showed that $n_e(Z,t)$ follows the n_A distribution almost exactly so that it will be approximated as:

$$n_e(h,t) = G(t)\exp\left\{-\frac{h}{e} - 6e^{-\frac{h}{e}}\right\} = G(t)\,f(h) \qquad \text{8-(5)}$$

Combining equations 8-(5) and 8-(3)

$$dI = -I\left[Q(n_a(h,0) - G(t))f(h) + \sigma n_{co_2}\right]p\,csc^2\lambda\,d\lambda \qquad \text{8-(6)}$$

now from 7-(1)

$$dI = -I\left[Qf(h)(k - G(t)) + \sigma n_{co_2}\right]p\,csc^2\lambda\,d\lambda \qquad \text{8-(7)}$$

so that

$$\int_{I_o}^{I}\frac{dI}{I} = -\int_{o}^{\chi}\left[Qf(h)(k - G(t)) + \sigma n_{co_2}\right]p\,csc^2\lambda\,d\lambda \qquad \text{8-(8)}$$

or .

$$I = I_o\,exp\left\{-\int_{o}^{\chi}\left[Qf(h)(k - G(t)) + \sigma n_{co_2}\right]p\,csc^2\lambda\,d\lambda\right\} \qquad \text{8-(9)}$$

where   h = pcscλ - R

Now the rate of production of electrons is

$$P = -\Delta\left.\frac{dI}{ds}\right|_{z} \qquad \text{8-(10)}$$

where Δ is the number of electrons released per photon absorbed for

ionization. Equation 8-(9) then becomes

$$P = \Delta I \left[Q \left(n_A(z,o) - G(t) f_{(z)} \right) \right] \qquad \text{8-(11)}$$

or

$$P = \Delta I_o \left[Q(n_A(z,o) - G(t) f_{(z)}) \right] exp \left\{ -\int_0^\lambda f_{(\lambda)} (k - G(t)) + \delta n_{co_2} p cse^2 d\lambda \right\} \quad \text{8-(12)}$$

where h = pcscλ - R

Since the ionization cross section and the solar flux are both wavelength dependent, the probability of ionization can be written as

$$p_r = \int_{\lambda_1}^{\lambda_2} Q I_o d\lambda$$

where Q is the absorption cross section and I_o is the solar flux per unit wavelength. For alkali metals Q varies from about 10^{-22} to 10^{-18} cm^{-2} (refs. 69,70). Integrating over wavelength, P becomes

$$p_r \approx 3 \times 10^{-8} sec^{-1} \text{ to } 3 \times 10^{-4} sec^{-1}$$

where (λ_1, λ_2) = (1900 A^o, 2700 A^o),

and these values, which are roughly the same as those for earth (ref. 71), are used for QI_o in Equation 8-(12).

The time dependent term in the production term is the variable χ (solar zenith angle). The variable χ is related to ϕ (local time measured from noon), by

$$Cos\,\chi = sin\,D\,sin(LA\,\pi) + Cos\,D\,Cos(LA\,\pi)\,cos\,\phi \qquad \text{8-(13)}$$

where D is the declination of the sun, LAI is the latitude at point P at height Z and

$$t = \frac{88775\,\phi}{2\pi} = 1.41 \times 10^{4}\,\phi \quad , \text{ since there are} \qquad \text{8-(14)}$$

88775 seconds in the Martian solar day.

The conditions for the sun not to be visible at point P are

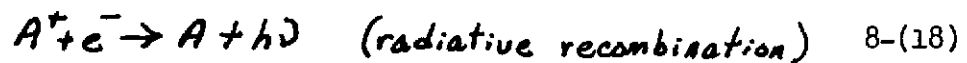$$Cos\,\chi < 0 \qquad AND \quad \left| (1 + {}^{2}/_{R})sin\,\chi \right| < 1 \qquad \text{8-(15)}$$

and if these are met

$$P \equiv O \qquad \text{8-(16)}$$

There were two types of loss reactions considered. The first is radiative recombination in which the ionized material recombines directly with an electron. This type of reaction is schematically
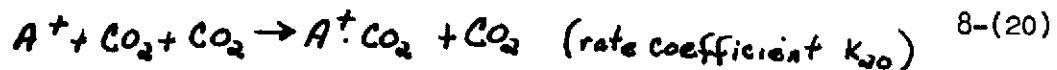
$$A + h\nu \rightarrow A^+ + e^- \qquad (production)$$

8-(17)

and

$$A^+ + e^- \rightarrow A + h\nu \qquad (radiative\ recombination)$$

8-(18)
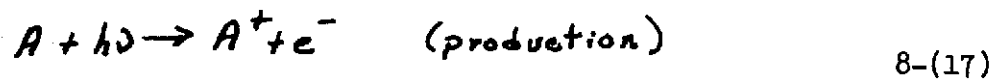
If the atmosphere is electrically neutral, this reaction has a loss term of

$$L = -\alpha n_e^2$$

8-(19)

The second type of loss reaction is a more complicated process in the atmosphere, such as

$$A + h\nu \rightarrow A^+ + e^- \qquad (production)$$

8-(17)

followed by the two-step process

$$A^+ + CO_2 + CO_2 \rightarrow A^+ \cdot CO_2 + CO_2 \qquad (rate\ coefficient\ k_{20})$$

8-(20)

and

$$A^+ \cdot CO_2 + e^- \rightarrow A + CO_2 \qquad (rate\ coefficient\ k_{21})$$

8-(21)

A second reaction of the same type is the process:

$$A^+ + M \rightarrow A^+ \cdot M \qquad (\text{rate coefficient } k_{82})$$

8-(22)

$$A^+ \cdot M + e^- \rightarrow AM \qquad (\text{rate coefficient } K_{23})$$

8-(23)
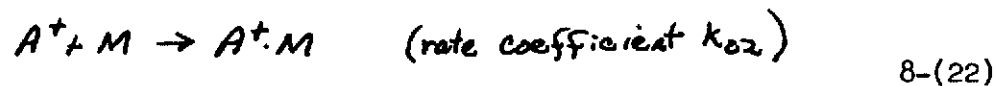
Reaction pair (18-19) are called CO_2 clustering (ref. 67) and reaction pair (20-21) would be using as dust particle as a recombination center, such as suggested previously (ref. 68). In both reactions (20-21) and (22-23), if the rate constants are such that

$$K_{20} (n_{co_2})^2 \gg K_{21} n_e$$

or

$$K_{22} n_m \gg K_{23} n_e$$

then the loss process can again be characterized by Equation (17),

$$L = -\alpha n_e^2$$

8-(19)

The value of α varies greatly, depending on whether the loss process is only radiative recombination or some combination of the processes discussed above. The range of values used here is from

2×10^{-12} cm^{3}sec^{-1} to 10^{-6} cm^{3}sec^{-1} (refs. 71,72,73,74).

Finally, the production and loss terms are combined into the simplified continuity equation to yield,

$$\frac{d n_e}{d t} = P - L \qquad \qquad 8\text{-}(24)$$

or combining with Equation 8-(14)

$$\frac{d n_e}{d \phi} = (1.41 \times 10^{4})(P - L) \qquad \qquad 8\text{-}(25)$$

where P is defined by Equation 8-(12), L by Equation 8-(19), and the relation of λ to ϕ by Equation 8-(13).

. A computer program was developed to solve Equation 8-(25). Inputs to the program are, height in the atmosphere, latitude, sun declination angle and constants for the production rate, loss rate, and alkali number density. The program starts with zero initial electron density and integrates Equation 8-(25) forward in time, using the final electron density of the previous day as the starting condition for the successive day.

The differential Equation 8-(25) is integrated by a fifth-order integration subroutine. The classical fourth-order Runge-Kutta formula is applied in conjunction with Richardson's Extrapolation to the Limit Theory. The subroutine is a variable interval size routine in which the interval is varied to meet a specified local relative truncation error. A second subroutine is used to compute the integral

in the production function (Equation 8-(12)). The current values of all variables, as updated from the differential equation subroutine, are used in a ten point Gauss Quadrature integration subroutine. The accuracy of these subroutines is far better than is required for the problem at this time, since the accuracy of the parameters characterizing the electron layer are order of magnitude.

At the end of three Martian days, the results were printed and compared. If convergence,

$$\frac{n_e(t' + \text{one day}) - n_e(t')}{n_e(t' + \text{one day})} \approx 10^{-3},$$

had occurred, the results were plotted; if not, then the program was continued from the last computing point or new intial conditions were imposed and the program rerun.

CHAPTER IX. Approximate Solution of Some Equations of Interest

In order to both obtain an estimate of what effect the variation of coefficients (such as the absorption and recombination coefficients) would do to the electron layer, and to reduce the range and time of the computer runs, several approximations to the previously described equations were developed. The first was developed to approximate the maximum electron density. In order to do this, two approximations were made in the electron production term (Equation 8-(12)); that the effect of CO_2 absorption was negligible ($\sigma \lesssim 10^{-22} cm^{-2}$); and that, since the alkali layer has a small number density (characterized by the parameter K) and such a small absorption cross section that the product QK is sufficiently small enough to drop the exponential time dependence term in Equation 8-(12). Since the maximum electron density will occur when $\frac{dN_e}{dt} = 0$ (if reached), then

$$I_o \left[Q \left(n_A - n_{e_{max}} \right) \right] = \alpha \, n_{e_{max}}^2 \qquad \qquad 9\text{-}(1)$$

so that if $\quad R \equiv \dfrac{\int_{\lambda_1}^{\lambda_2} Q I_o \, d\lambda}{\alpha}$

$$\qquad \qquad 9\text{-}(2)$$

$$n_{e_{max}}(z) = \frac{R}{2} \left[\sqrt{1 + \frac{4 n_A(z)}{R}} - 1 \right] \qquad \qquad 9\text{-}(3)$$

From Equation 9-(3) (under the same assumptions as Equation 9-(1)) can also be found the required alkali concentration for a given maximum electron density, i.e.,

$$n_A(z) = \frac{n_{e_{max}}^2(z) + R\, n_{e_{max}}(z)}{R} \qquad 9\text{-}(4)$$

The second equation is the decline in the electron number density after the sun sets. The differential equation is

$$\frac{d n_e}{d t} = -\alpha n_e^2 \qquad 9\text{-}(5)$$

the solution of which is

$$n_e(z,t) = \frac{n_e(z,t_o)}{1 + \alpha n_e(z,t_o)(t-t_o)} \qquad 9\text{-}(6)$$

or rewritten

$$\alpha = \frac{\dfrac{n_e(z,t_o)}{n_e(z,t)} - 1}{n_e(z,t_o)[t - t_o]} \qquad 9\text{-}(7)$$

Equations 9-(4) and 9-(7) will be used later to narrow the range of acceptable coefficients. The final results to be presented, however, are based on the numerical solutions to Equation 8-(25).

CHAPTER X. Results and Discussion of the Study

All of the computer simulations were run at a latitude of 45° and

a sun declination angle of 0° (corresponding to summer or winter

solstice). On the basis of the considerations discussed in Section

VIII, the range of the absorption cross section was 10^{-22} to 10^{-18}

cm^2 and the range of the recombination coefficients was from 2×10^{-18}

to 10^{-6} $cm^3 sec^{-1}$.

Table I and Table II list the coefficients for each model and the

electron densities for each model at eight altitudes in the atmosphere.

In Table I there are two electron densities listed for each model at

each altitude. The upper entry is the expected peak equilibrium

electron density as obtained from approximation Equation 9-(3). The

lower entry is the actual maximum electron density as computed from

the time-dependent equations. Again, in Table II there are two elec-

tron densities listed for each model at each altitude. In Table II

the upper number corresponds to the expected minimum electron density

obtained by using Equation 9-(6), and the lower number is the minimum

computed electron density as computed from the time-dependent equa-

tions. Some general observations can be made from these tables.

These observations will be shown in further detail in the following

figures. The first is that Equation 9-(3) gives a reasonable approxi-

mation for the peak value of the electron number density, and, as

is shown in equation 9-(3), the larger the value of R, $(R = \alpha^{-1} \int Q I_0 d\lambda)$,

the larger the peak electron number density. The second observation is

that the smaller the value of αn_e, the less the nighttime decay of

the electron density as was predicted by equation 9-(6).

Figure 6a and 6b are plots of the electron density for Model 0. Model 0 has constants of $\alpha = 2 \times 10^{-12}$ cm^3 sec^{-1}, $Q = 10^{-22}$ cm^2, and $K = 9.78 \times 10^5$ cm^{-3}. In Figure 6a are plotted the electron density versus hour angle for eight altitudes in the atmosphere. The hour angle is related to the time of day by Equation 8-(13). Examples of local times are $\phi = -90^\circ$ is approximately sunrise, $\phi = 0$ is local noon, $\phi = 90^\circ$ is approximately local sunset, and $\phi = \pm 180^\circ$ is midnight. Figure 6b is a plot of electron density versus altitude for the four times just illustrated. Model 0 has a large value of R and also has a large peak electron density, 2×10^4 cm^{-3}. This model has the smallest value of α/Q and thus the electron density exhibits an almost imperceptible nighttime decay. The lack of decay is exhibited in Figure 6b, where the profiles for the four times of day all lie on each other. The initial condition for Model 0 was zero electrons per cm^3, but it was converging so slowly that the computation was restarted using electron densities slightly lower than the values obtained from Equation 9-(3). This procedure, in effect, moves time forward in a large step and results in a convergence of $\Delta n/n$ between morning terminators of about 10^{-4}.

Model 1 ($\alpha = 2 \times 10^{-12}$ cm^3 sec^{-1}, $Q = 10^{-18}$ cm^2, and $K = 9.78 \times 10^5$) results are plotted in Figures 7a and 7b. The value of R for Model 1 is very large and this should result in a large electron density, which did occur and is shown in Figure 7a.

Again the value of αn_e is small and the variation of electron density is very small, which results in all four time curves apparently coinciding in Figure 7b. Model 1 converged in about a week of Martian time.

Model 2 ($\alpha = 10^{-6}$ cm^3 sec^{-1}, $Q = 10^{-22}$ cm^2, $K = 9.78 \times 10^5$ cm^{-3}) is the first model that shows a day/night electron density variation of the type needed to explain the diurnal pressure variation. It shows a diurnal equilibrium, i.e., the cycle repeats daily, but it does not exhibit an equilibrium in the sense that the time derivative of the electron density equals zero. This can be seen in Figure 8a, where there is a large discontinuity in d_{ne}/dt at the terminators, no equilibrium concentration is reached, and yet diurnal equilibrium is established. Model 2 has a small value of R, which is exhibited by the extremely low electron densities achieved (on the order of 1/500 of the electron densities of Model 0, for example). The value of αn_e is in the midrange of those investigated, resulting in the slow decay in the density distribution during the night. This can be seen in Figure 8b which is the first model to exhibit diurnal variation of the electron profile. Model 2 was slow to converge and convergence was difficult to determine because of the small numerical value of electron density.

Model 3 ($\alpha = 10^{-6}$ cm^3 sec^{-1}, $Q = 10^{-18}$ cm^2, $K = 9.78 \times 10^5$ cm^{-3}) completes the extremes of Q and α investigated, and also exhibits the third type of diurnal variation encountered in the investigation.

This diurnal variation is evident in Figure 9a, where there is a very sharp rise in electron density at sunrise, which is a result of the large value of Q, and equilibrium of dn_e/dt being zero is reached during the sunlight hours, and then a very sharp decay in the electron density at night, which is a result of the large value of αn_e. From Figure 9b, the profile plot for Model 3, it can be seen that for the midrange value of R, the peak electron density is not too very large, but the large diurnal variation in electron density, which is required to explain the pressure differences, is present. Model 3 reached equilibrium in about 6 days of Martian time.

To complete this preliminary analysis, the mid-range values of $Q = 10^{-22}$ cm^2 and $\alpha = 10^{-8}$ cm^3 sec^{-1} were investigated. Model 6 ($\alpha = 10^{-8}$ cm^3 sec^{-1}, $Q = 10^{-22}$ cm^2, $K = 9.78 \times 10^5$ cm^{-3}) results are plotted in Figures 10a and 10b. The value of R is small, which results in low electron number density as can be seen in Figure 10a. The value αn_e was also small, which implies slow decay, which is exhibited in both Figures 10a and 10b. Model 6 reached equilibrium after about 30 diurnal cycles.

The results of Model 7 ($\alpha = 10^{-8}$ cm^3 sec^{-1}, $Q = 10^{-18}$ cm^2, $K = 9.78 \times 10^5$ cm^3) are plotted in Figures 11a and 11b. The recombination coefficient α is such that αn_e is large and thus the distribution should exhibit a pronounced nighttime decay, and this decay can be seen from Figure 11a. The value of R for Model 7 is also large and therefore the peak electron number density is large as shown in Figure 11b.

Examination of the foregoing results indicates that the sinu-
soidal diurnal variation of the electron density which is observed in
the earth's ionosphere is not duplicated by this low-lying electron
layer on Mars. This is predominately due to the affect of the product
of the absorption cross section (low) and the source number density
(very low) being a very small number. When this product is small the
exponential term in the electron production Equation 9-(3), which ac-
counts for the time variation, is very weak. Therefore, even for the
long slant paths at the terminators, the ionizing radiation on Mars
has only been slightly attenuated. In fact, the production function,
for the low-lying electron, can be thought of almost as a light switch
having two positions—on and off.

. The second result of this study came after the conclusion of all
the actual time dependent calculations. The result was that Equation
9-(3), which neglected time dependence, gave a good approximation to
the peak electron number density (6 % average error). Thus as more and
better data about the Martian atmosphere become available, equation
9-(3) can be used to give a quick approximation as to the effect of
the low-lying electron layer on the atmospheric properties deduced by
radio occultation and vice versa.

The third result was that the larger the value of αn_e the
faster the nighttime decay of the electron density. This would be ex-
pected from an examination of Equation 9-(6). The general trend was
that for values of $\alpha n_e < 10^{-6} \sec^{-1}$ the distribution showed no
diurnal variation; for values $10^{-4} \sec^{-1} > \alpha n_e > 10^{-6} \sec^{-1}$, the

distribution exhibited a sawtooth variation; and for $\alpha n_e > 10^{-4}$ sec^{-1}, a sharp rise and fall or square wave.

Combining the results of the foregoing study with the measured pressure data should allow the possible range of the various coefficient to be narrowed. From the discussion of pressure data is Section IV, it is clear that the peak electron density must be on the order of 6×10^4 electrons per cm^3, and that this number must decrease at night to the point of being undetectable. To determine the recombination coefficient Equation 9-(7) is used

$$\alpha = \frac{\frac{n_e(z,t_o)}{n_e(z,t)} - 1}{n_e(z,t_o)[t - t_o]}$$

9-(7)

with n_e (10.75 Km, sunset) $\approx 6 \times 10^4$ cm^{-3}, {t - t sunset} $\approx$ 2 hours and n_e (10.75 Km, t) $\approx 6 \times 10^3$ cm^{-3}, which is an electron density low enough to be masked by an experiment error of 4% at the pressure levels in question. For these values, the resulting recombination coefficient must be on the order of 2×10^{-8} cm^3 sec^{-1} ; for ease of calculation let $\alpha = 10^{-8}$ cm^3 sec^{-1}. Then, to determine the required alkali source number density, Equation 9-(4) is rewritten with $n_A(z) = Kf(z)$

$$K = \frac{n^2_{e_{max}}(z) + R\, n_{e_{max}}(z)}{R\, f(z)}$$

where $f(z) = \exp \{ - (z/6 + 6e^{-z/6}) \}$ and $R = \alpha^{-1} \int QI_o d\lambda$. There-
fore assuming $Q = 10^{-18}$ cm^2, K is of the order of 2.92×10^6 cm^{-3},
which means a peak density of alkali atoms of 1.79×10^5 cm^{-3}. Having
a 0.2 micron particle sublimate 1/10,000 of its mass in alkali atoms
would require a dust distribution of only 9 particles per cm^3 in order
to produce the required alkali atom density. One outcome of this
study, then, is that the coefficients of $\alpha = 10^{-8}$ cm^3 sec^{-1}, $Q = 10^{-18}$
cm^2 and $K = 2.92 \times 10^6$ cm^{-3}, which are within the range of laboratory
measurements of the processes involved, should produce an electron
density model which will explain the apparent diurnal pressure varia-
tion. These coefficients are used in Model 8, and the computed elec-
tron densities are plotted in Figures 12a and 12b. The effect of the
larger cross section can be seen in Figure 12a as the extremely rapid
rise in the electron density immediately after sunrise. The electron
density reaches an equilibrium of about 6×10^4 electrons per cm^3, as
required, for the entire daylight period. The medium large product of
αn_e produces a rapid nighttime decay as is shown in Figures 12a and
12b. From Figure 12b can be seen the electron density height profiles
for four different times in the Martian day. The morning profile has
already nearly 90 percent of the equilibrium density shortly after
sunrise. The noon and evening profiles coincide at the equilibrium
densities. Finally the extremely rapid decay can be seen as the mid-
night profile has fallen to 1/100 of the equilibrium density.

XI. Conclusions

There are some general conclusions about the low-lying electron layer distribution that can be inferred from this study. First, because the product of the absorption cross section and the number density of the ionized constituent is small, the production term in the continuity equation has very little daylight time dependence. The result of this lack of time dependence is that the sinusoidal time variation in electron density that is observed on earth is not present in the low altitude electron distribution. Second, the value of αn_e determines the shape of the electron density versus time curves; and thus, for electron layers that are of possible importance in the explanation of the radio occultation pressure discrepancies, the value of αn_e must be at least equal to or greater than about 10^{-4} sec^{-1}. Third, for $\alpha n_e \geq 10^{-4}$ sec^{-1}, Equation 9-(3) gives a good approximation to the peak electron density daytime distribution.

From the preliminary radio occultation data, it has been found that the following values for the coefficients used in this study would adequately account for a 1 mb difference between day and night pressures: $\alpha = 10^{-8}$ cm^3 sec^{-1}, $Q = 10^{-18}$ cm^2 and $K = 2.92 \times 10^6$ cm^{-3}.

This value of the absorption coefficient is in the range of that measured for the alkali metals. The value of the recombination coefficient ($\sim 10^{-8}$ cm^3 sec^{-1}) implies that radiative recombination is not the dominant process for the loss of electrons. The possible loss mechanism that the dust acts as a recombination site, recombination

rate unknown, is also not very probable since the dust density is numerically so small. Thus, the most probable mechanism for the loss of electrons is that of CO_2 clustering to the alkali ion (ref. 67), which has a very high rate coefficient.

Finally, because of an analysis of the following factors: a low altitude residual dust layer in the Martian atmosphere has been observed and measured and is theoretically required to explain temperature lapse rates; this dust will be composed of alkali and alkali compounds having low ionization potentials; and the Martian atmosphere has low concentrations of O, O_2, and O_3 allowing solar ultraviolet radiation to penetrate to the planet's surface, it is concluded that there will be a low altitude electron layer. This study has shown that it is well within the range of possible conditions in the atmosphere to obtain peak electron densities on the order of 6×10^4 electrons cm^{-3}, which would be required to explain the observed diurnal pressure difference.

XII. Suggestions for Future Research

Several areas of research are available at the present time utilizing currently available data. The first is a comprehensive reanalysis of present Martian atmospheric pressure data to determine if the effects of the low altitude electron layer are of sufficient magnitude to be able to more closely define the physical properties of the layer. Secondly, studies can be initiated towards a simple analysis of meteoric ablation. These studies would give an idea as to

how closely an equilibrium distribution of ablated particles matches the required aerosol concentration layer. Differences between the two, if any, would give a starting point as to the amount of aerosols that must be lifted into the Martian atmosphere by meteorological phenomena.

Finally, it is proposed that this low altitude electron layer should be searched for and examined by some experiment. The discovery and understanding of such a layer would not only be useful in the study of the Martian atmosphere but would also aid in the modeling of the poorly understood earth's alkali metal ion region and sporadic E layer, since the Martian analysis would be much simpler (because of the much simpler Mars atmosphere). For example, several models of the earth's alkali layer involve wind induced $\vec{V} \times \vec{B}$ shear layers of charged dust particles as a source of alkali atoms or involve wind induced $\vec{V} \times \vec{B}$ layers as a removal mechanism for the alkali ion (ref. 75). Thus, on Mars where the magnetic field is less than 10^{-3} that of the earth, the analysis of the effects of the lack of large magnitude $\vec{V} \times \vec{B}$ forces in the alkali layer formation would have direct bearing on earth models requiring such forces.

Two experiments which could be utilized to detect the low altitude electron layer are a two-frequency radio occultation experiment or a twilight glow phenomena experiment. The two-frequency radio occultation experiment (currently planned for the Viking orbiter) will yield two values for the index of refraction of the Martian atmosphere because of the different probing frequencies (see Equation 4-(1)).

The subtraction of the two indices of refraction and the knowledge of the frequencies will yield a close approximation to the electron number density (since the index of refraction of most low density neutral gases is not very wavelength dependent). The twilight glow experiment would be to search for emission lines in the atmospheric twilight. The identification of lines allows the delineation of the alkali species and the intensity of the line can be related to the species number density. Such an experiment could be implemented on an orbiting spacecraft and could quite likely be combined with some similar type of emission experiment.

Appendix A

This appendix is a short derivation of the steps needed to arrive at equations 4-1 and 4-3 in section IV. To derive equation 4-1, it is assumed at first that in an electrically neutral, non-conducting (no free electrons) atmosphere of dielectric constant ϵ_n, one of Maxwells equations can be written as

$$A(1) \qquad \nabla \times \vec{H} = \epsilon_n \frac{\partial \vec{E}}{\partial t}$$

If now the electrically neutral medium contain free electrons (density n_e) in addition to the neutral part of the medium, then the conducting part of the medium can be characterized by a conductivity σ and Maxwells equation is supplemented by Ohm's law

$$A(2) \qquad \vec{J} = \sigma \vec{E} = n_e (e^-) \vec{V}$$

where $\vec{V}$ is the velocity of electron

so that

$$A(3) \qquad \nabla \times \vec{H} = \epsilon_n \frac{\partial \vec{E}}{\partial t} + \vec{J}$$

    or

$$A(4) \qquad \nabla \times \vec{H} = \epsilon_n \frac{\partial \vec{E}}{\partial t} + \sigma \vec{E}$$

If it is assumed that the right hand side can be expressed as some composite dielectric coefficient times $\frac{\partial \vec{E}}{\partial t}$ to reduce the

equation to the simple form of eq. (1) then A(5) $\nabla \times \vec{H} = \varepsilon_n \frac{\partial \vec{E}}{\partial t} + \sigma \vec{E}$ $= \varepsilon_c \frac{\partial \vec{E}}{\partial t}$. To determine the conductivity, assume that there are negligible collisions so that the equation of motion of an electron is

A(6) $\qquad m \frac{d\vec{V}}{dt} = e^- \vec{E}$

A(7) now if $\vec{E} = E_o e^{-i\omega t}$

A(8) $\qquad \vec{V} = \frac{i e^-}{\omega m} \vec{E}$

from A(2)

A(9) $\qquad \sigma \vec{E} = n_e e^- \vec{V} = \frac{i n_e (e^-)^2}{\omega m} \vec{E}$

so that

A(10) $\qquad \sigma = \frac{i n_e (e^-)^2}{\omega m}$

substituting A(10) into A(5)

A(11) $\qquad \varepsilon_n \frac{\partial \vec{E}}{\partial t} + \left(\frac{i n_e (e^-)^2}{\omega m} \right) \vec{E} = \varepsilon_c \frac{\partial \vec{E}}{\partial t}$

or

A(12) $\qquad -i \omega \varepsilon_n + \frac{i n_e (e^-)^2}{\omega m} = -i \omega \varepsilon_c$

or rearranged

A(13) $\qquad \epsilon_c = \epsilon_n - \dfrac{n_e\,(e^-)^2}{\omega^2 m} = \epsilon_n - \dfrac{n_e}{m}\left(\dfrac{e^-}{4\pi f}\right)^2$

If the magnetic field is small such that the magnetic permeability of the medium is approximately that of free space, then $\mu \equiv \sqrt{\dfrac{\epsilon}{\epsilon_o}}$ is the real index of refraction and

A(14) $\qquad \mu_c^2 = \mu_n^2 - \dfrac{n_e\,(e^-)^2}{(4\pi)^2 \epsilon_o m\, f^2}$

which is equation 4-1.

To arrive at equation 4-3 in the text, define

A(15) $\qquad \chi \equiv \dfrac{n_e\,(e^-)^2}{(4\pi)^2 \epsilon_o m\, f^2}$

then, equation A-14 becomes

A(16) $\qquad \mu_c^2 = \mu_n^2 - \chi$

Now the index of refraction of just the electrons is

A(17) $\qquad \mu_e^2 = \left(1 + N_e\,x\,10^{-6}\right)^2 = 1 - \chi$

A(18) so that $1 + N_e \times 10^{-6} = \sqrt{1 - x} \approx 1 - \dfrac{1}{2}x$

or

A(19) $$N_e \times 10^{-6} \approx -\frac{1}{2} X$$

substituting A(16) into A(19)

A(20) $$N_e \times 10^{-6} \approx \frac{1}{2}\left(\mu_c^2 - \mu_n^2\right) = \frac{1}{2}\left(\mu_c - \mu_n\right)\left(\mu_c + \mu_n\right)$$

A(21) Now $\mu_c + \mu_n \approx 2$

A(22) and $$\mu \equiv 1 + N \times 10^{-6}$$

so that A-20 becomes

A(23) $$N_e \times 10^{-6} \approx \frac{1}{2}\left(1 + N_c \times 10^{-6} - 1 - N_n \times 10^{-6}\right)(2)$$

A(24) $$N_e \approx N_c - N_n$$

which is equation 4-3 in the text.

1. Leighton, R. B., et al., Television Observations from Mariners 6
    and 7, Mariner-Mars 1969, NASA SP-225, p. 37.

2. Masursky, Harold, et al., Mariner 9 Television Reconnaissance of
    Mars and Its Satellites: Preliminary Results. Science 175,
    January 21, 1972, pp. 294.

3. Leovy, C. B., et al., The Martian Atmosphere: Mariner 9 Television
    Experiment Progress Report, ICARUS 17, 2, 1972, p. 373.

4. Herr, K. C. and Pimentel, G. C., Infrared Spectroscopy, Mariner-Mars
    1969, NASA SP-225, p. 83.

5. Hanel, R. A., et al., Infrared Spectroscopy Experiment on the
    Mariner 9 Mission: Preliminary Results, Science 175, January 21,
    1972, p. 305.

6. Hanel, R. A., et al., Investigation of the Martian Environment by
    Infrared Spectroscopy on Mariner 9, ICARUS 17, 2, 1972, p. 423.

7. Neugebauer, G., et al., Infrared Radiometry, Mariner-Mars 1969,
    NASA SP-225, p. 105.

8. Chase, S. C., et al., Infrared Radiometry Experiment on Mariner 9,
    Science 175, January 21, 1972, p. 308.

9. Barth, C. A., et al., Mariner 9 Ultraviolet Spectrometer Experiment:
    Mars Airglow Spectroscopy and Variations in Lyman Alpha, ICARUS 17,
    2, 1972, p. 457.

10. Barth, C. A., et al., Mariner 9 Ultraviolet Spectrometer Experiment:
    Initial Results, Science 175, January 21, 1972, p. 309.

11. Barth, C. A., et al., Ultraviolet Spectroscopy, Mariner-Mars 1969,
    NASA SP-225, p. 97.

12. Stewart, A. I., et al., Mariner 9 Ultraviolet Spectrometer Experi-
    ment: Structure of Mars' Upper Atmosphere, ICARUS 17, 2, 1972, p. 469.

13. Fjeldbo, G. and Eshleman, U. R., The Atmosphere of Mars Analyzed by
     Integral Inversion of the Mariner IV Occultation Data, Planet. Space
     Sci. 16, 1968, p. 1035.

14. Rasool, S. I., et al., Temperature Distributions in the Lower Atmo-
     sphere of Mars from Mariner 6 and 7 Radio Occultation Data, J. Atmos.
     Sci. 27, 1970, p. 841.

15. Rasool, S. I. and Stewart, R. W., Results and Interpretation of the
     S-Band Occultation Experiments on Mars and Venus, J. Atmos. Sci. 28,
     1971, p. 869.

16. Kliore, A. J., et al., Mariner 9 S-Band Martian Occultation Experi-
     ment: Initial Results on the Atmosphere and Topography of Mars,
     Science 175, January 21, 1972, p. 313.

17. Kliore, A. J., et al., The Atmosphere of Mars from Mariner 9 Radio
     Occultation Measurements, ICARUS 17, 2, 1972, p. 484.

18. Hogan, J. S., et al., Results of the Mariners 6 and 7 Mars Occulta-
     tion Experiment, NASA TN D-6683, March 1972.

19. Kliore, A. J., et al., S-Band Radio Occultation Measurements of the
     Atmosphere and Topography of Mars with Mariner 9: Extended Mission
     Coverage of Polar and Intermediate Latitudes, J. Geophys. Res. 78,
     20, 1973, p. 4331.

20. Harrington, J. V.; Grossi, M. D.; and Langworthy, B. M., Mars
     Mariner 4 Radio Occultation Experiment: Comments on the Uniqueness
     of the Results, J. Geophys. Res. 73, 9, 1968, p. 3039.

21. Jeffreys, H., The Earth. University Press, Cambridge, 1959.

22. Lorell, J., et al., Gravity Field of Mars from Mariner 9 Tracking
     Data Transactions, AGU 53, 4, 1972, p. 432.

23. Lorell, J., Mariner 9 Celestial Mechanics Experiment: Gravity Field
     and Pole Direction of Mars, Science 175, January 21, 1972, p. 317.

24. Runcorn, S. K., On the Implications of the Shape of Mars, ICARUS 18,
     1973, p. 109.

25. Schubert, G. and Lingenfelter, R. E., Martian Center of Mass — Center of Figure Offset, Nature 242, March 1973, p. 251.

26. Michael, W. H. Jr.; Wallio, H. A.; and Levine, J. S.: Mars Lower Atmosphere: Some New Implications, COSPAR Paper No. k.7, Madrid, Spain, May 10-24, 1972.

27. Belton, M. J. S. and Hunter, D. M., The Distribution of CO_2 on Mars: A Spectroscopic Determination of Surface Topography, ICARUS 15, 1971, p. 204.

28. McElroy, M. B., Structure of Venus and Mars Atmospheres, J. Geophys. Res. 74, 1, 1969, p. 29.

29. Cloutier, P. A.; McElroy, M. B.; and Michel, F. C., Modification of the Martian Ionosphere by the Solar Wind, J. Geophys. Res. 74, 26, 1969, p. 6215.

30. Stewart, R. W., The Electron Distribution in the Mars and Venus Upper Atmospheres, J. Atmos. Sci. 28, Sept. 1971, p. 1069.

31. Gringauz, K. I., and Breuss, T. K., Comparative Cha acteristics of the Ionospheres of the Planets of the Terrestrial Group: Mars, Venus, and Earth, Space Science Rev. 10, 1970, p. 743.

32. Kolosov, M. A., et al., Preliminary Results of the Investigation of the Martian Atmosphere with the Mars-2 Satellite, Dokl. Nauk SSSR 206, 5, 1972, p. 10171.

33. Whitten, R. C.; Poppoff, I. G.; and Sims, J. S., The Ionosphere of Mars Below 80 km Altitude - I, Planet. Space Sci. 19, 1971, p. 243.

34. Whitten, R. C., et al., The Ionosphere of Mars Below 80 km - II, Planet Space Sci. 19, 1971, p. 971.

35. Koval, I. K., The Martian "Crest," Priroda 4, 1972, p. 2.

36. Herzberg, G., Molecular Spectra and Molecular Structure, III. Electronic Spectra and Electronic Structure of Polyatomic Molecules, von Nostraud Reinhold Co., New York.

37. Koval, I. K., Atmosphere and Surface of Mars, Solar System Research 5, 3, 1972, p. 107.

38. Koval, I. K., The Martian "Crest," Priroda 4, 1972, p. 2.

39. Hanel, R. et al., Investigations of the Martian Environment by Infrared Spectroscopy on Mariner 9, NASA GSFC X-620-72-280, 1972.

40. Masursky, H., et al., Mariner 9 Television Reconnaissance of Mars and Its Satellites: Preliminary Results, Science 175, January 21, 1972, p. 294.

41. Watts, R. N., Some Mariner 9 Observations of Mars, Sky and Telescope 43, 1972, p. 208.

42. Moroz, V. I., et al., Dust Storms on Mars According to Photometric Observations Taken On-Board the Mars-3 Automatic Interplanetary Station, Kosm. Issled, (USSR) 10, 6, 1972, p. 925.

43. Moroz, V. I., The Mars-2 and Mars-3 Orbital Spacecraft: Results of Studies of the Surface and Atmosphere of Mars, NASA TTF-14,908, April 1973.

44. Leovz, C. B., et al., Mariner Mars 1969: Atmospheric Results, J. Geophys. Res. 76, 2, 1971, p. 297.

45. Gierasch, P. J. and Goody, R. M., The Effect of Dust on the Temperature of the Martian Atmosphere, J. Atmos. Sci. 29, 1972, p. 400.

46. Whitten, R. C. and Sims, J. S., The Photolytic Stability of the Martian Atmosphere, Planet. Space Sci. 21, 1973, p. 1333.

47. Moroz, V. I. and Ksanfomaliti, L. V., Preliminary Results of the Astrophysical Observations of Mars from AIS Mars-3, Fifteenth Plenary Meeting of COSPAR, Paper No. k.37, Madrid, Spain, May 1972.

48. Smith, R. E., Space and Planetary Environment Criteria Guidelines for Use in Space Vehicle Development, NASA TM X-64627, November 1971.

49. Borodin, L. S., Alkaline Locks: Indicators of the Earth's Interior, Priroda 5, May 1971, p. 62.

50. Gierasch, P. J. and Goody, R. M., A Study of the Thermal and Dynamical Structure of the Martian Lower Atmosphere, Planet. Space Sci. 16, 1968, p. 615.

51. Gierasch, P. J. and Sagan, C., A Preliminary Assessment of Martian Wing Regimes, ICARUS 14, 1971, p. 312.

52. Leovy, C. B., et al., The Martian Atmosphere: Mariner 9 Television Experiment Progress Report, ICARUS 17, 1972, p. 373.

53. Gierasch, P. J. and Goody, R. M., A Model of a Martian Great Dust Storm, J. Atmos. Sci. 30, 2, 1973, p. 169.

54. Gadsden, M., Sodium in the Upper Atmosphere: Meteoric Origin, J. Atmos. and Terr. Phys. 30, 1968, p. 151.

55. Elterman, L.; Toolin, R. B.; and Essex, J. D., Stratospheric Aerosol Measurements with Implications for Global Climate, Applied Optics 12, 2, 1973, p. 330.

56. Cox, S. K., et al., Measurements of Absorbed Shortwave Energy in a Tropical Atmosphere, Solar Energy 14, 1973, p. 169.

57. Cunmold, D. M.; Gray, C. R.; and Merritt, D. C., Stratospheric Aerosol Detection, J. Geophys. Res. 78, 6, 1973, p. 920.

58. Graham, D. A.; Ichikawa, T.; and Kim, J. S., Observations of Sodium, Lithium, and Potassium Twilightglow at Moscow, Idaho, U.S.A., Annales de Géophysique 27, 1971, p. 483.

59. Hanson, W. B. and Donaldson, J. S., Sodium Distribution in the Upper Atmosphere, J. Geophys. Res. 72, 21, 1967, p. 5513.

60. Gadsden, M., Comparison of Radio-Meteor Rate with Abundance of Sodium in the Upper Atmosphere, Annales de Géophysique 27, 1971, p. 401.

61. Istomin, V. G., Magnesium and Calcium Ions in the Earth's Upper Atmosphere, NASA TT F-69, September 1961.

62. Donahue, T. M. and Meier, R. R., Distribution of Sodium in the Daytime Upper Atmosphere as Measured by a Rocket Experiment, J. Geophys. Res. 72, 11, 1967, p. 2803.

63. Hunter, D. M. and Wallace, L., Rocket Measurements of the Sodium Dayglow, J. Geophys. Res. 72, 1, 1967, p. 69.

64. Hunter, D. M., Spectroscopic Studies of the Twilight Airglow, Space Sci. Rev. 6, 1967, p. 493.

65. Gadsden, M., Metallic Atoms and Ions in the Upper Atmosphere, Annales de Géophysique 26, 1970, p. 141.

66. Visconti, G., Enhancement of Upper Atmospheric Sodium from Sporadic Dust Influxes, J. Atmos. and Terr. Phys. 35, 1973, p. 1331.

67. Keller, G. E. and Beyer, R. A., CO_2 and O_2 Clustering to Sodium Ions, J. Geophys. Res. 76, 1971, p. 289.

68. Zikmunda, J. and Mohnen, V. A., Ion Annihilation by Aerosol Particles from Ground Level to 60 km Height, Meteorologische Rundschan 25, 1972, p. 10.

69. Dichthum, R. W., et al., The Continuous Absorption of Light in Alkali-Metal Vapours, Proc. of the Royal Society, Series A, Mathematical and Physical Sciences 219, 1136, p. 89.

70. Samson, J. A. R., The Alkali Metals. In Advances in Atomic and Molecular Physics, Vol. 2, edited by Bates, D. R. and Estermann, I., Academic Press, New York, 1966.

71. Marneo, F. F.; Pressman, J.; and Aschenbrand, L. M., Artificial Electron Clouds - II, Planet. Space Sci. 1, 1969, p. 291.

72. Yadava, V. K.; Prasad, R. Y.; and Tolpadi, S. K., Magnesium and Associated Ionospheric Processes in E_s-layer Formation, Annales de Géophysique 28, 1972, p. 575.

73. Aikin, A. C. and Goldbug, R. A., Metallic Ions in the Equatorial Ionosphere, J. Geophys. Res. 78, 1973, p. 734.

74. Narcisi, R. S., Processes Associated with Metal-Ion Layers in the E Region of the Ionosphere, Space Research VIII, North-Holland Publishing Co., Amsterdam, 1967, pp. 360-369.

75. Lockheed Missile and Space Company, A Spectrum of New Experiments to Investigate Alkali Metal Chemistry in the E Region, RADC-TR-71-923, June 1971.

Model	Q (cm^2)	α $(cm^3 sec^{-1})$	K (cm^{-3})	R (cm^{-3})	n_e (cm^{-3})	0	5	10.75	15	20	30	40	50
0	E-22	2E-12	9.78E+05	1.51E+04		2126 / 2013	15491 / 14043	23502 / 20770	20719 / 18479	14427 / 13085	4804 / 4540	1148 / 1090	231 / 219
1	E-18	2E-12		1.51E+08		2424 / 2424	31323 / 31323	59940 / 59940	49041 / 49041	28161 / 28161	6328 / 6328	1235 / 1235	234 / 234
2	E-22	E-06		3.03E-02		8 / 6	30 / 29	42 / 41	38 / 37	29 / 27	13 / 12	6 / 4	2 / 1
3	E-18	E-06		3.03E+02		718 / 718	2933 / 2932	4113 / 4113	3706 / 3706	2773 / 2773	1241 / 1241	478 / 478	155 / 155
6	E-22	E-08		3.03		64 / 62	306 / 232	424 / 330	384 / 298	290 / 224	136 / 105	59 / 48	25 / 22
7	E-18	E-08		3.03E+05		2256 / 2256	19184 / 19182	30087 / 30085	26274 / 26273	17758 / 17758	5375 / 5375	1188 / 1188	232 / 232
8	E-18	E-08	2.92E+06	3.03E+05		6035 / 6035	40202 / 40197	60044 / 60040	53169 / 53167	37553 / 37552	13170 / 13170	3323 / 3323	685 / 685

Altitude (km) column headers: 0, 5, 10.75, 15, 20, 30, 40, 50

Table I. Predicted maximum electron densities (upper entry) and computed maximum electron densities (lower entry), for eight altitudes in the Model atmospheres.

Model	Q (cm²)	α (cm³ sec⁻¹)	K (cm⁻³)	αn_e (sec⁻¹)	n_e (cm⁻³) 0	5	10.75	15	20	30	40	50
0	E-22	2E-12	9.78E+05	4.7E-08	2125	15470	23454	20684	14410	4802	1148	231
					2013	14027	20735	18451	13071	4539	1090	219
1	E-18	2E-12		1.2E-07	2424	31241	59646	48846	28097	6325	1234	233
					2423	31241	59646	48847	28097	6324	1235	234
2	E-22	E-06		4.2E-05	6	17	15	15	13	9	4	1
					5	13	15	14	13	8	4	1
3	E-18	E-06		4.1E-03	22	24	24	24	24	25	24	22
					21	23	24	24	24	25	24	22
6	E-22	E-08		4.2E-06	81	27	361	331	260	130	58	24
					60	21	291	266	206	131	47	·22
7	E-18	E-08		3.0E-04	1128	2111	2248	2253	2192	1735	817	213
					1128	2111	2248	2229	2192	1736	817	214
8	E-18	E-08	2.92E+06	6.0E-04	1642	2240	2335	2355	2344	2145	1464	545
					1642	2239	2335	2355	2344	2145	1464	545

Table 2. Predicted morning electron densities (upper entry) and computed morning electron densities (lower entry), for eight altitudes in the Model atmospheres.
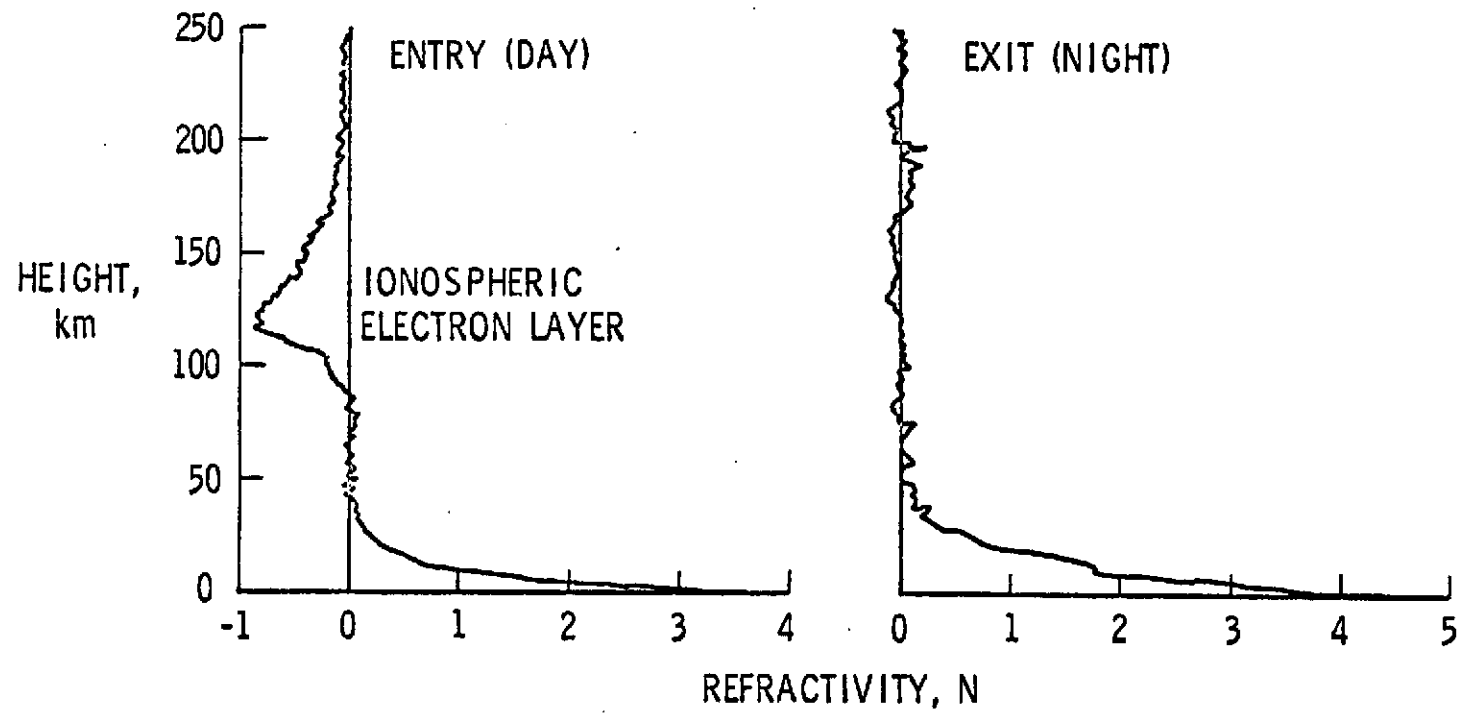
Figure I.   Sketch of typical atmospheric refractivity profiles for Mars.
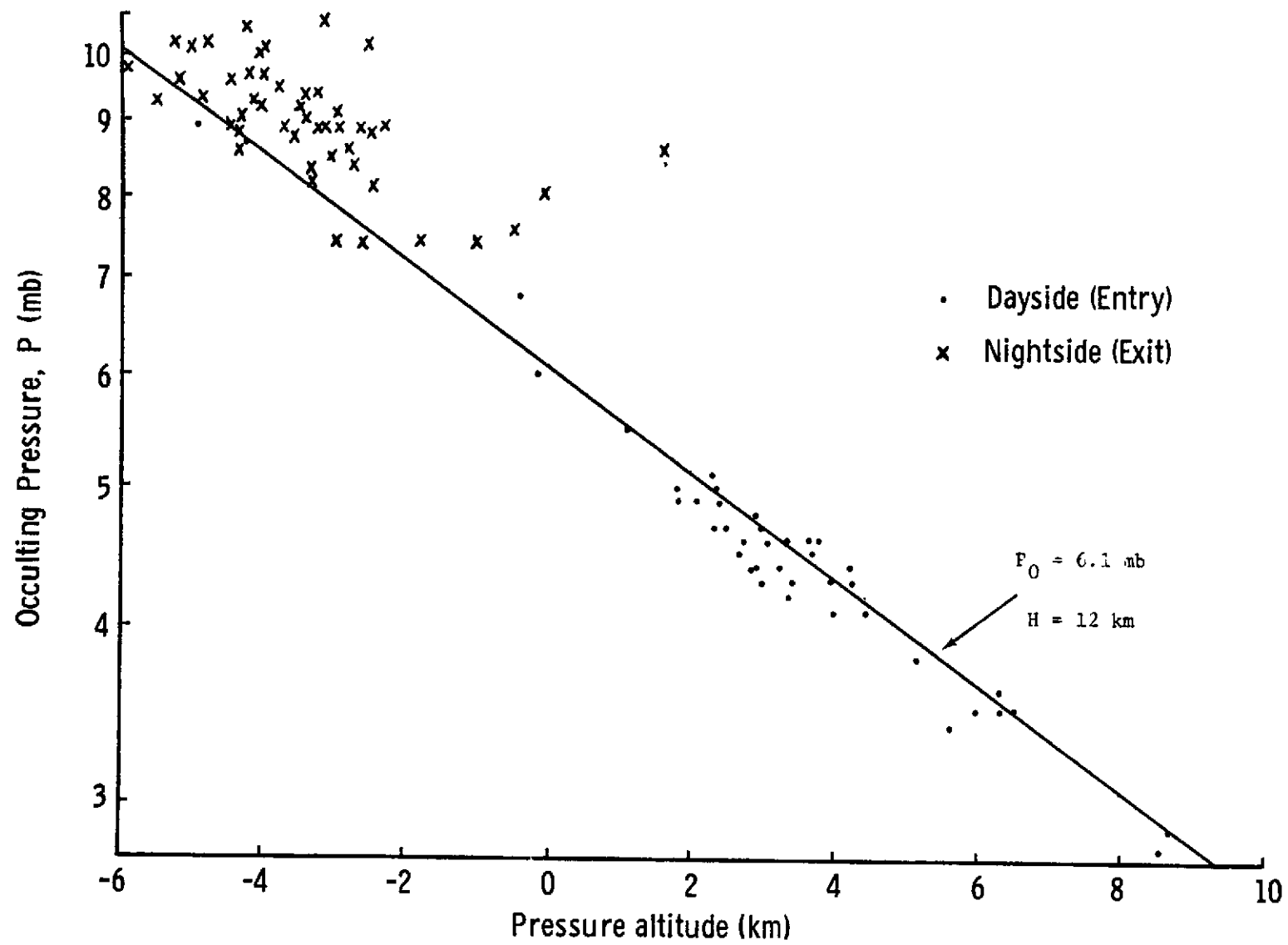
Figure 2. Dayside and nightside surface pressures plotted against pressure altitude.
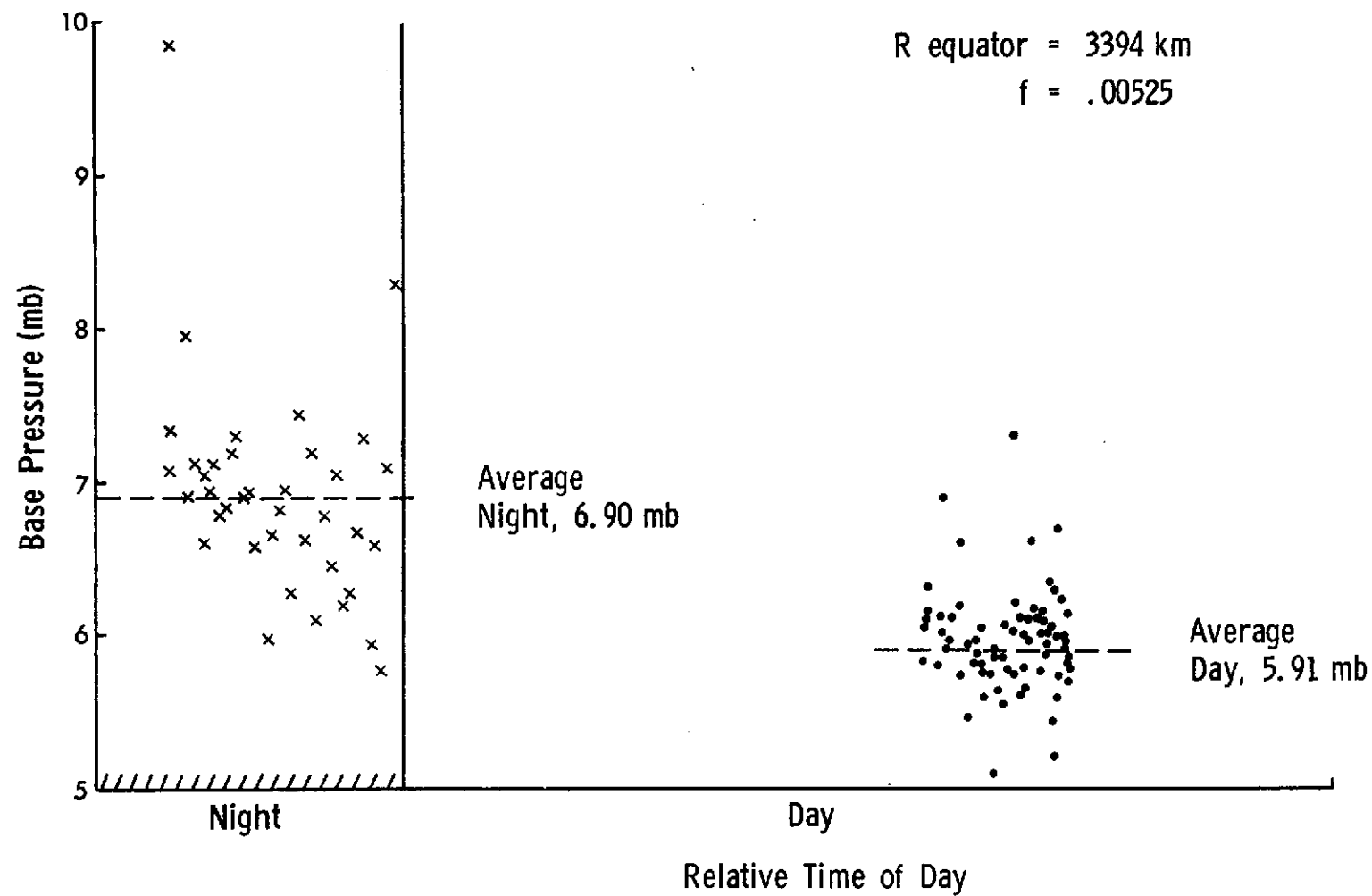
Figure 3. Martian base pressures from Mariner 9 radio occultation.
(Referenced to equipotential surface)
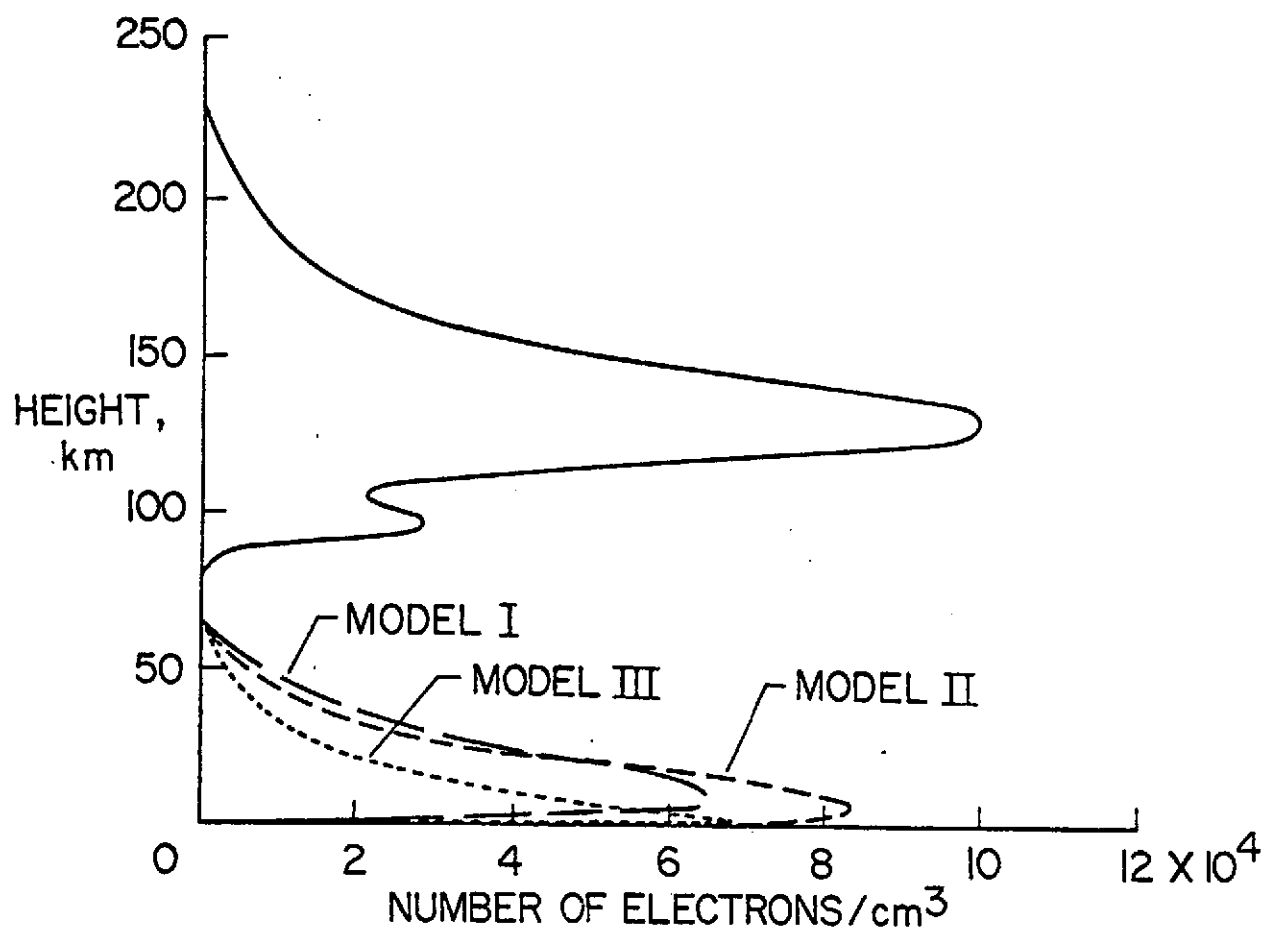
Figure 4. Calculated lower atmosphere electron density profiles.

$$p = (R+h) = (R+Z) \sin x$$

$$S = {}^-p \cot \lambda \quad \text{measured from } p$$

$$dS = p \csc^2 \lambda \, d\lambda$$

Figure 5.   Geometry used in the derivation of the electron production equation.
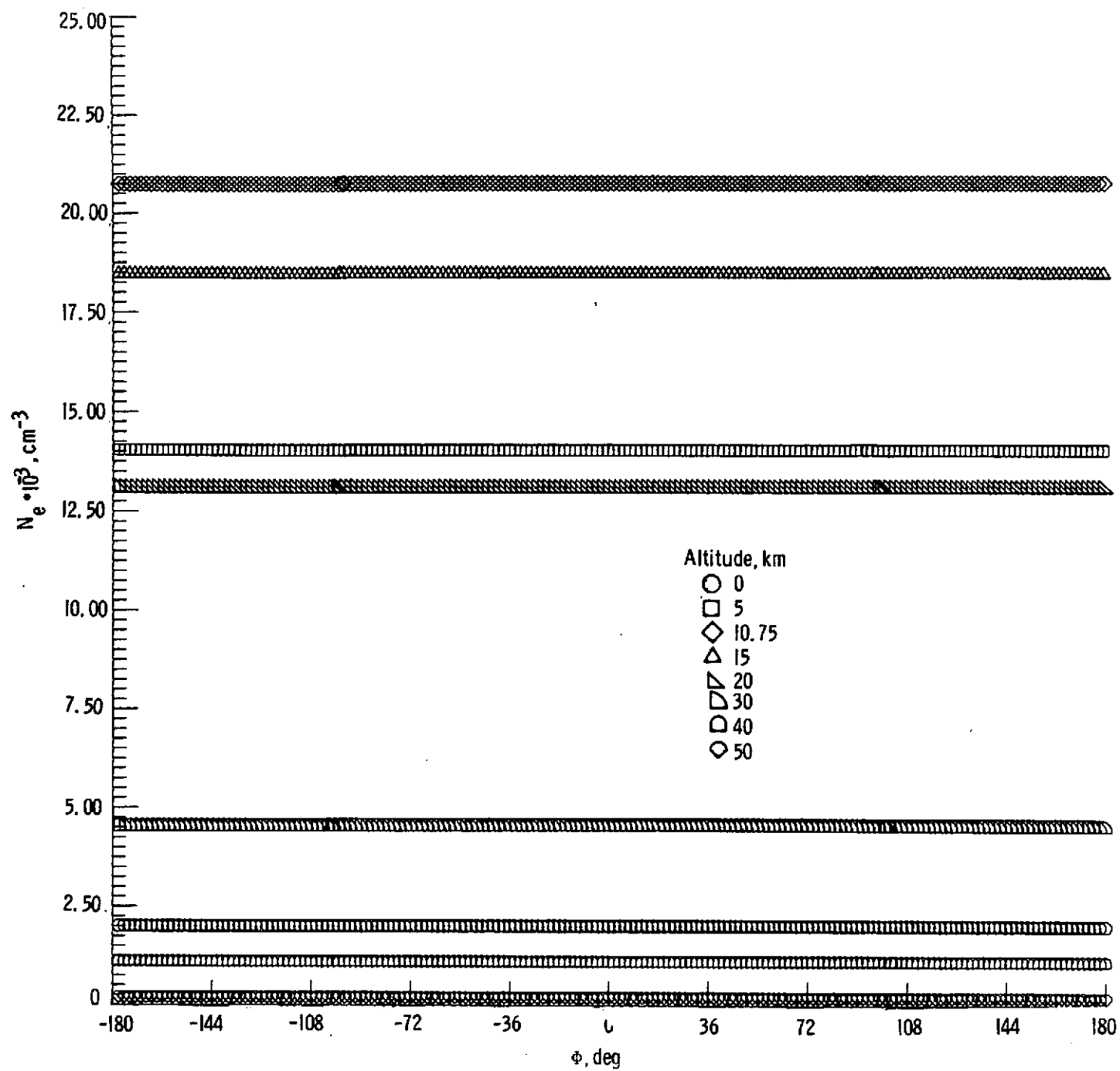
Figure 6a. Electron densities of Model 0 as a function of hour angle.
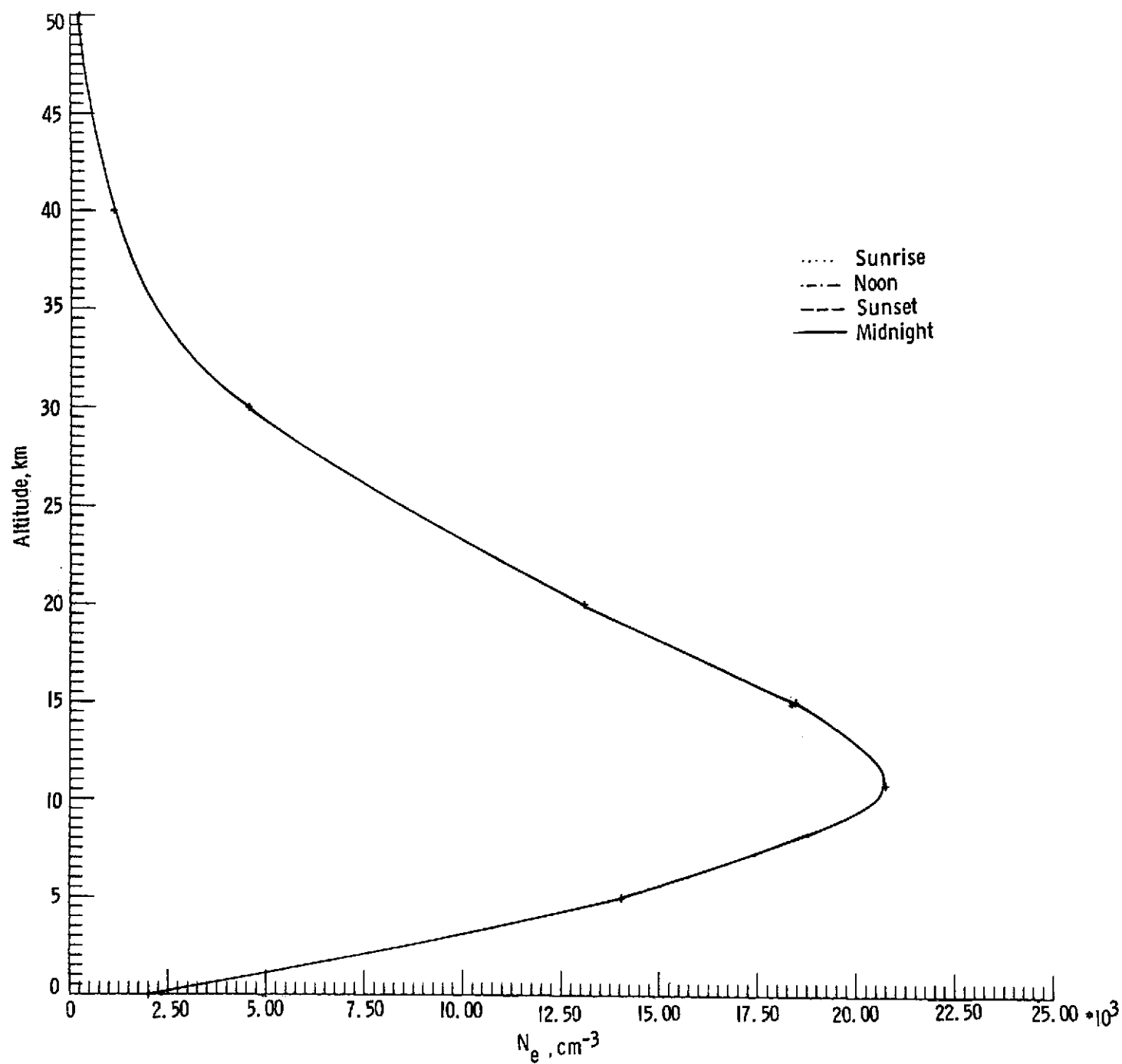
Figure 6b. Electron profile for Model 0.
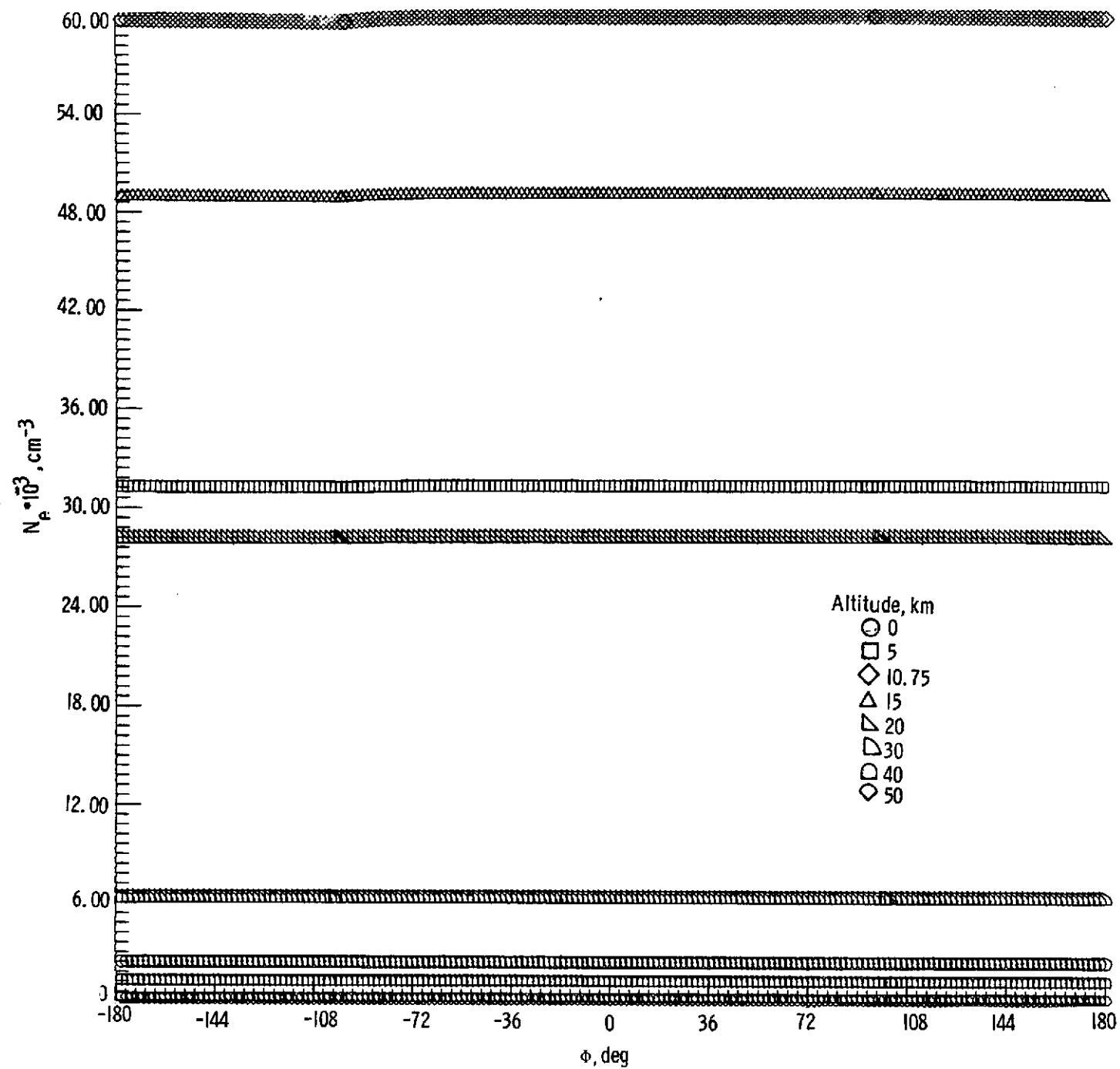
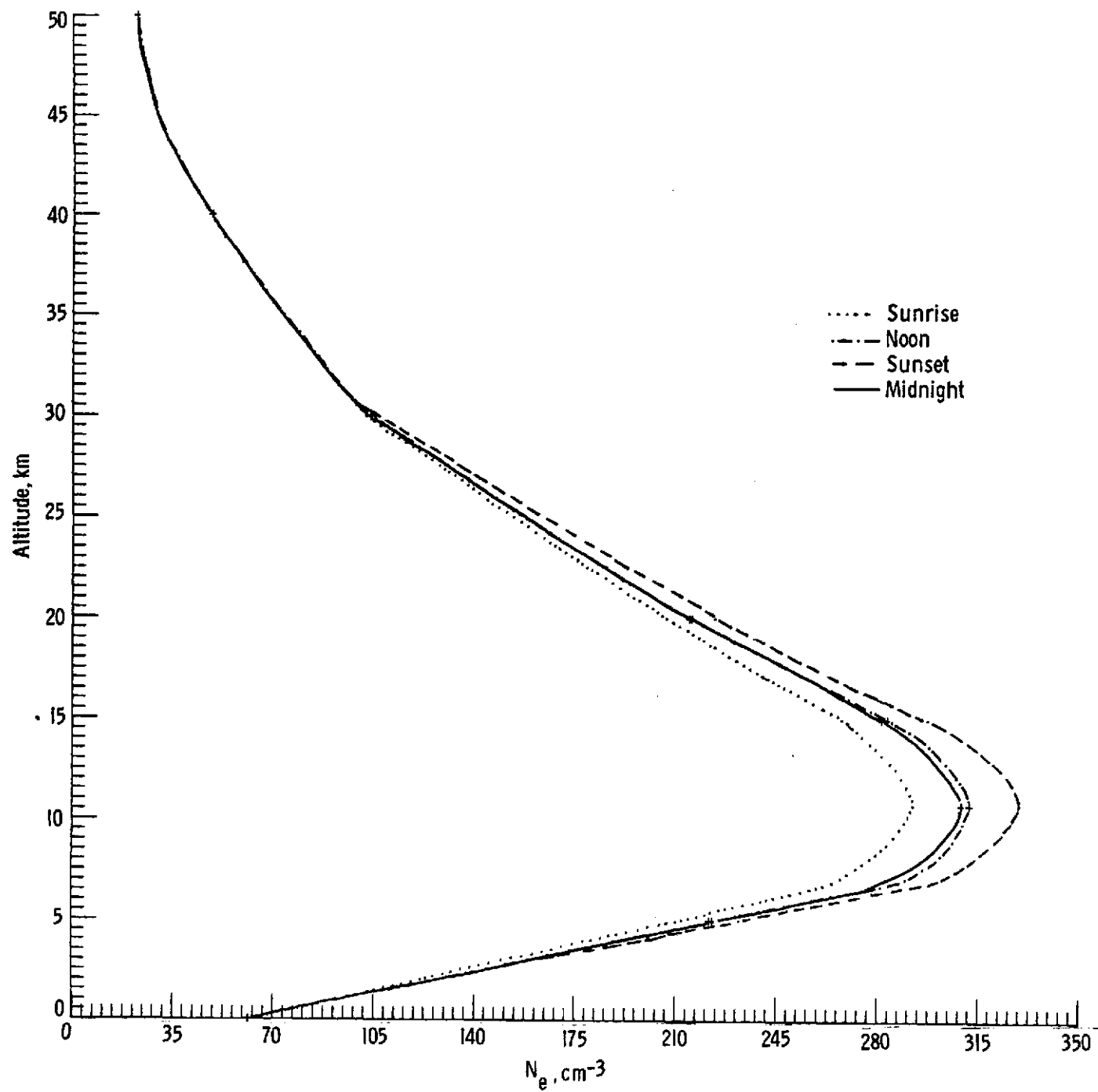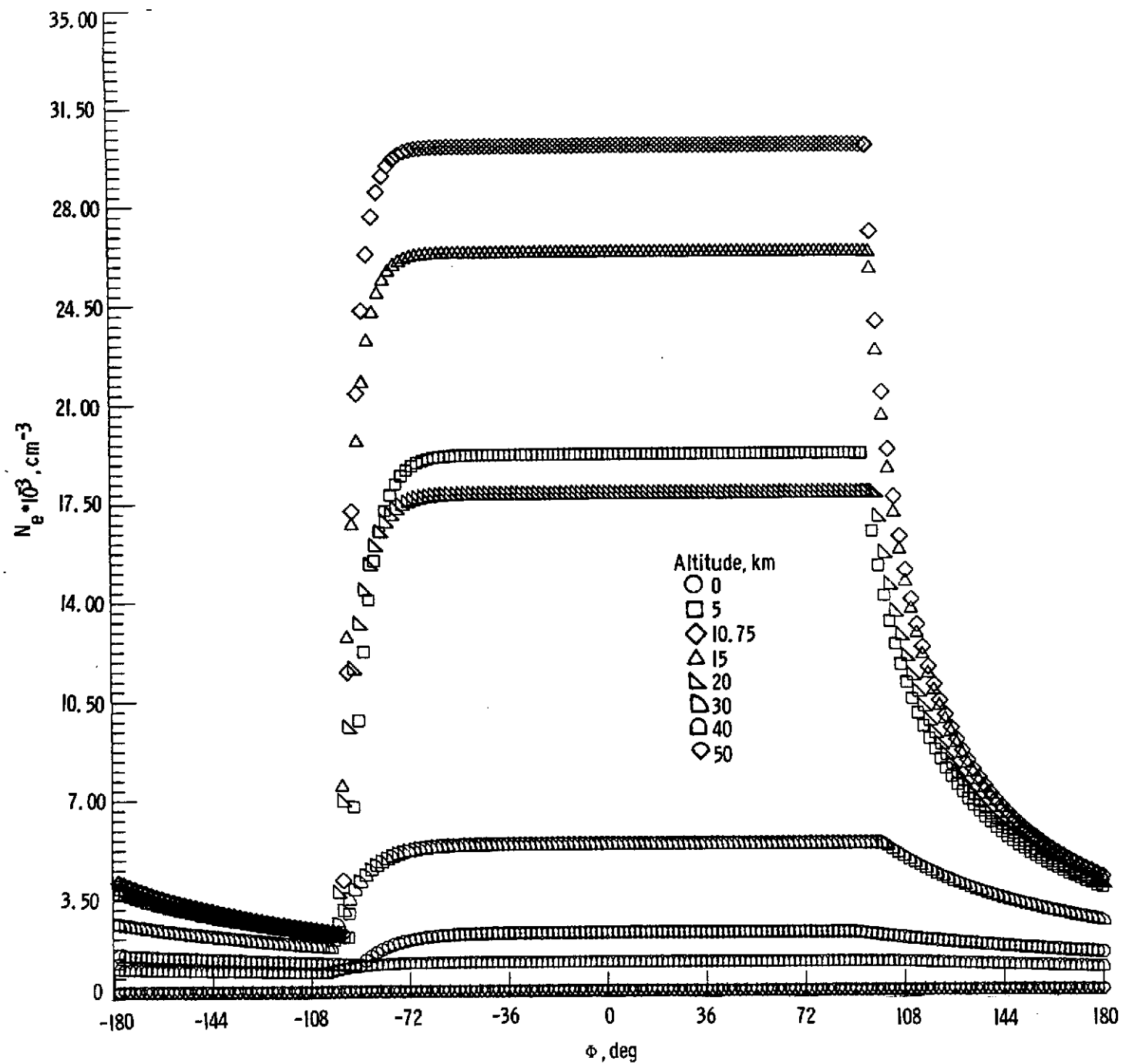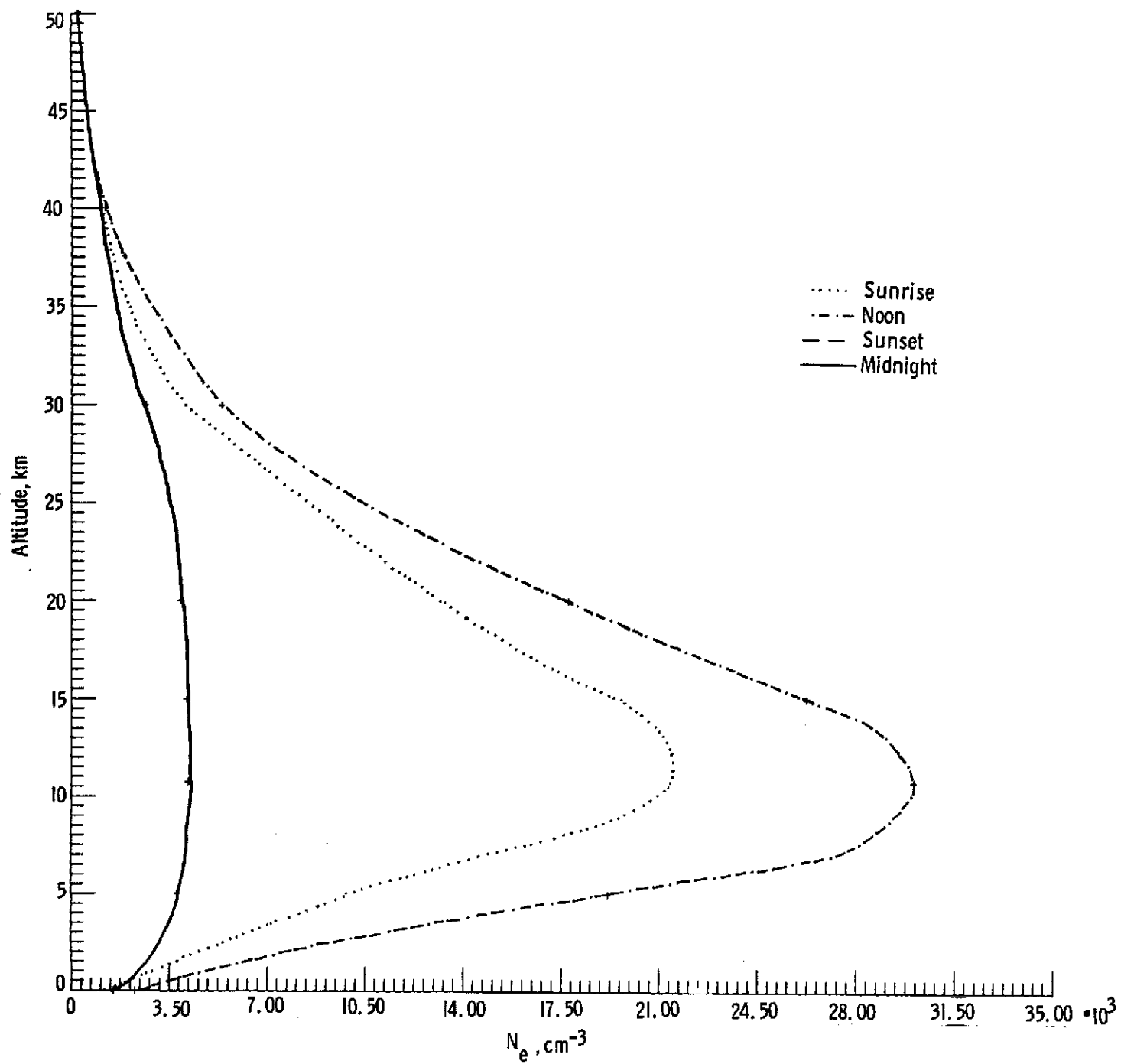Figure 7a. Electron densities of Model I as a function of hour angle.
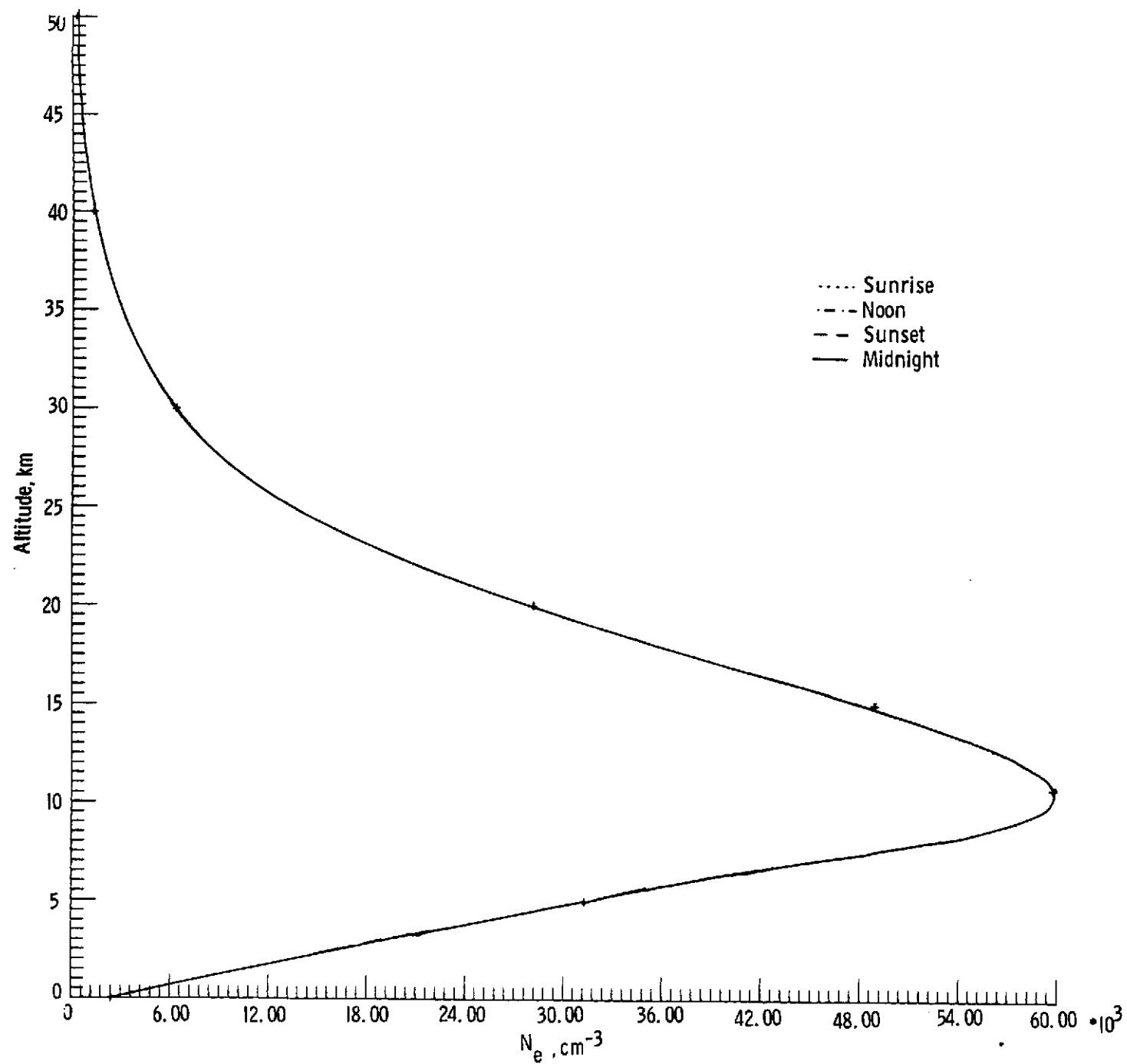
Figure 7b. Electron profile for Model I.
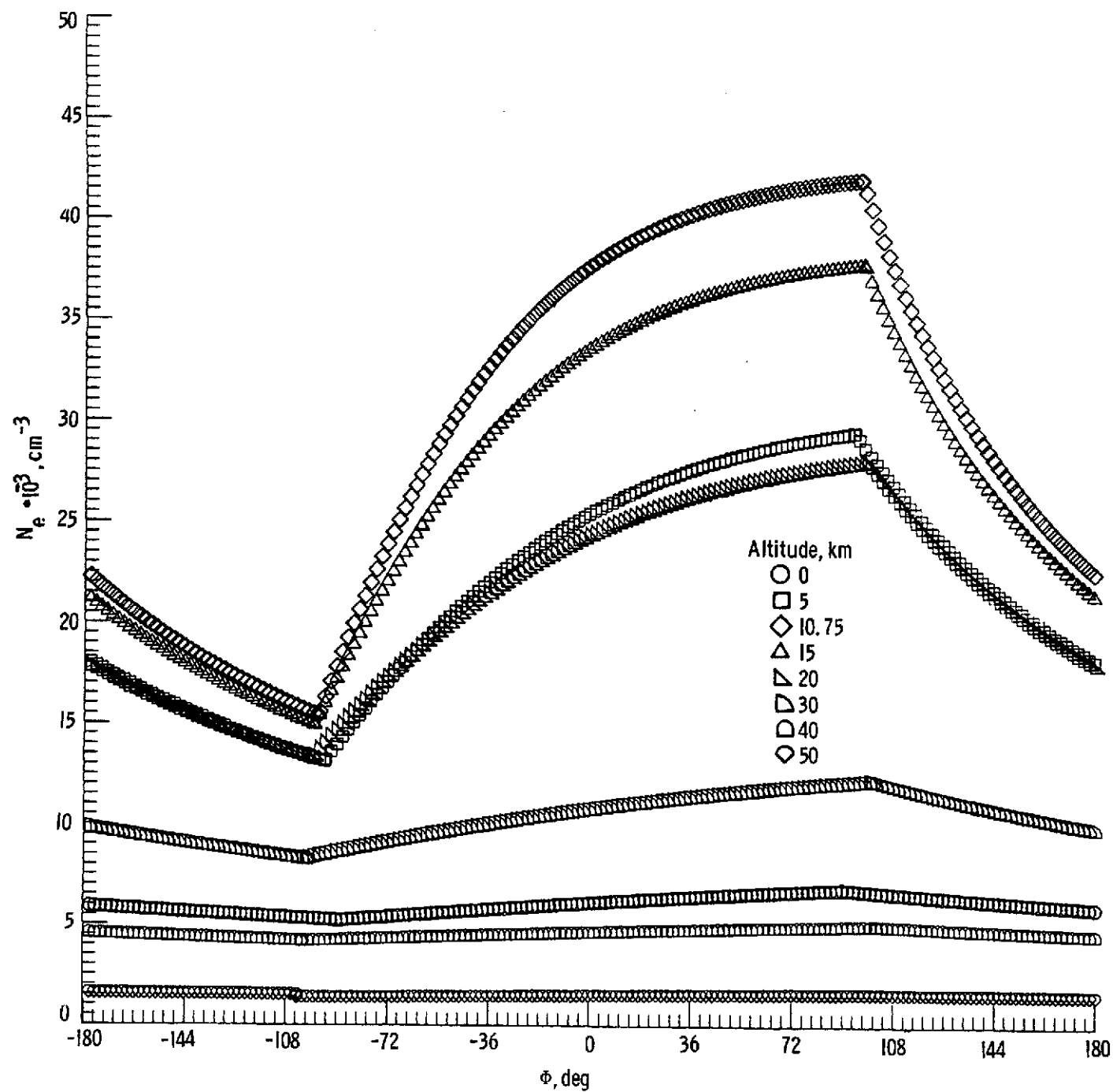
Figure 8a. Electron densities of Model 2 as a function of hour angle.
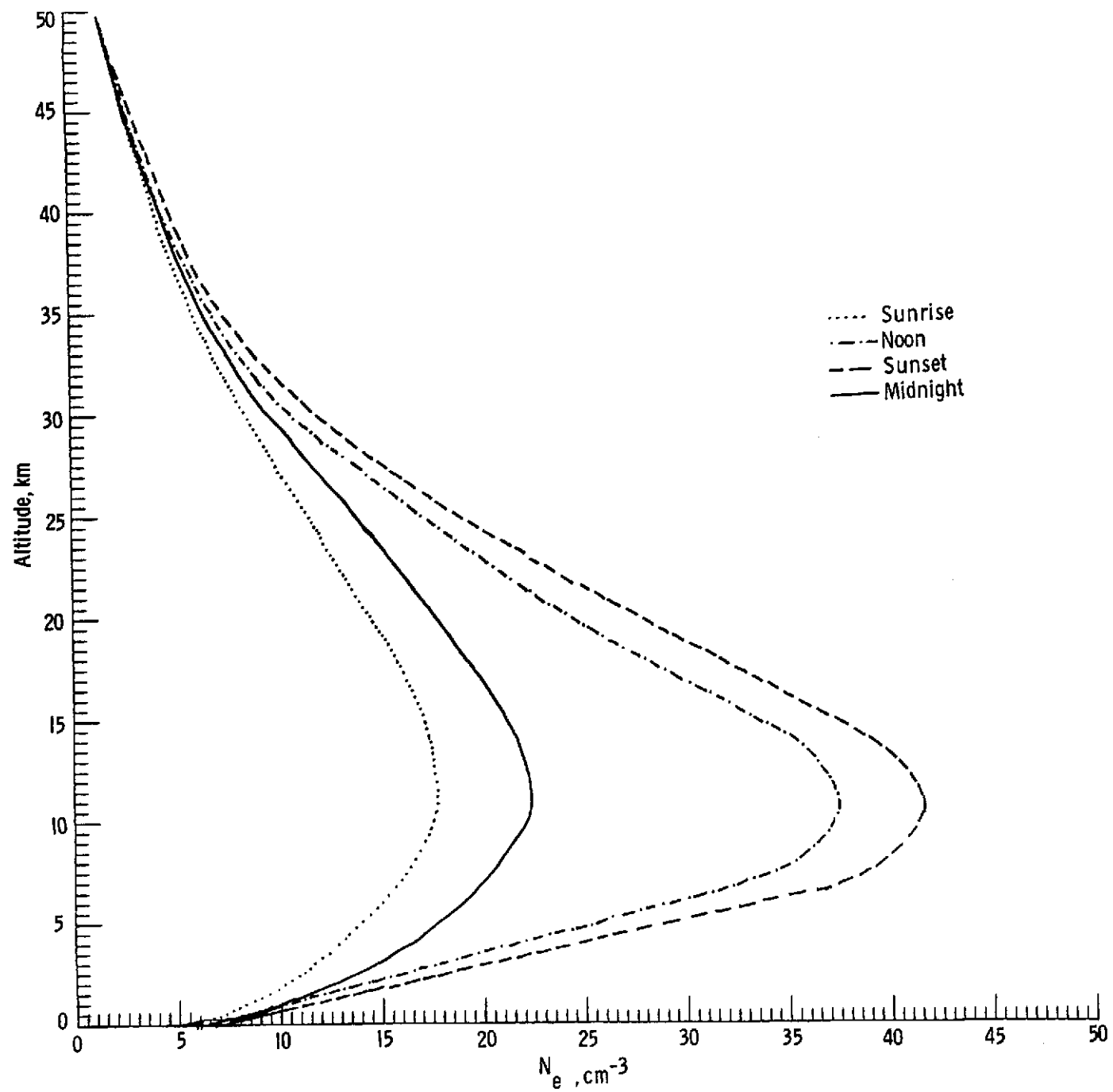
Figure 8b. Electron profile for Model 2.
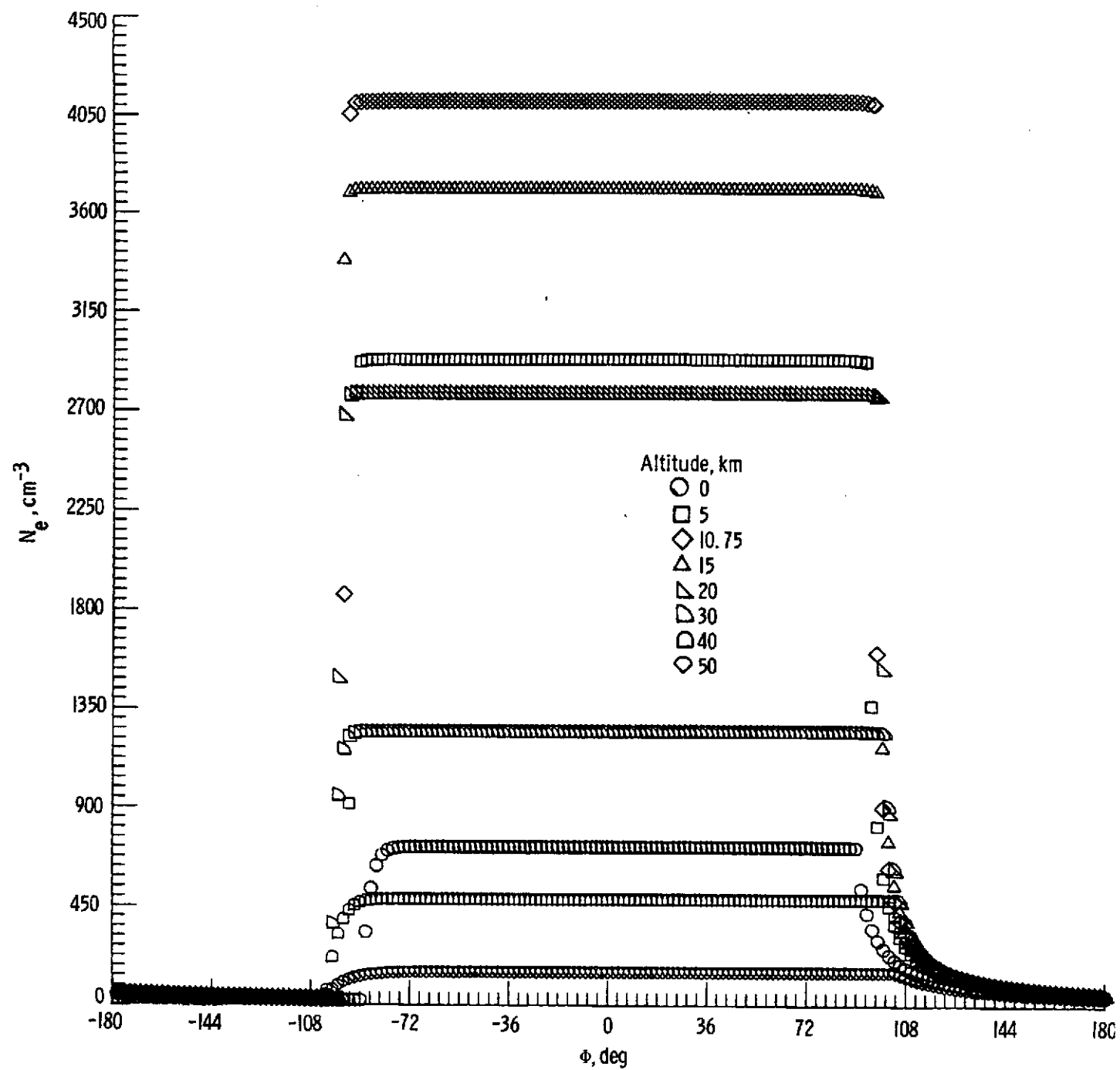
Figure 9a. Electron densities of Model 3 as a function of hour angle.
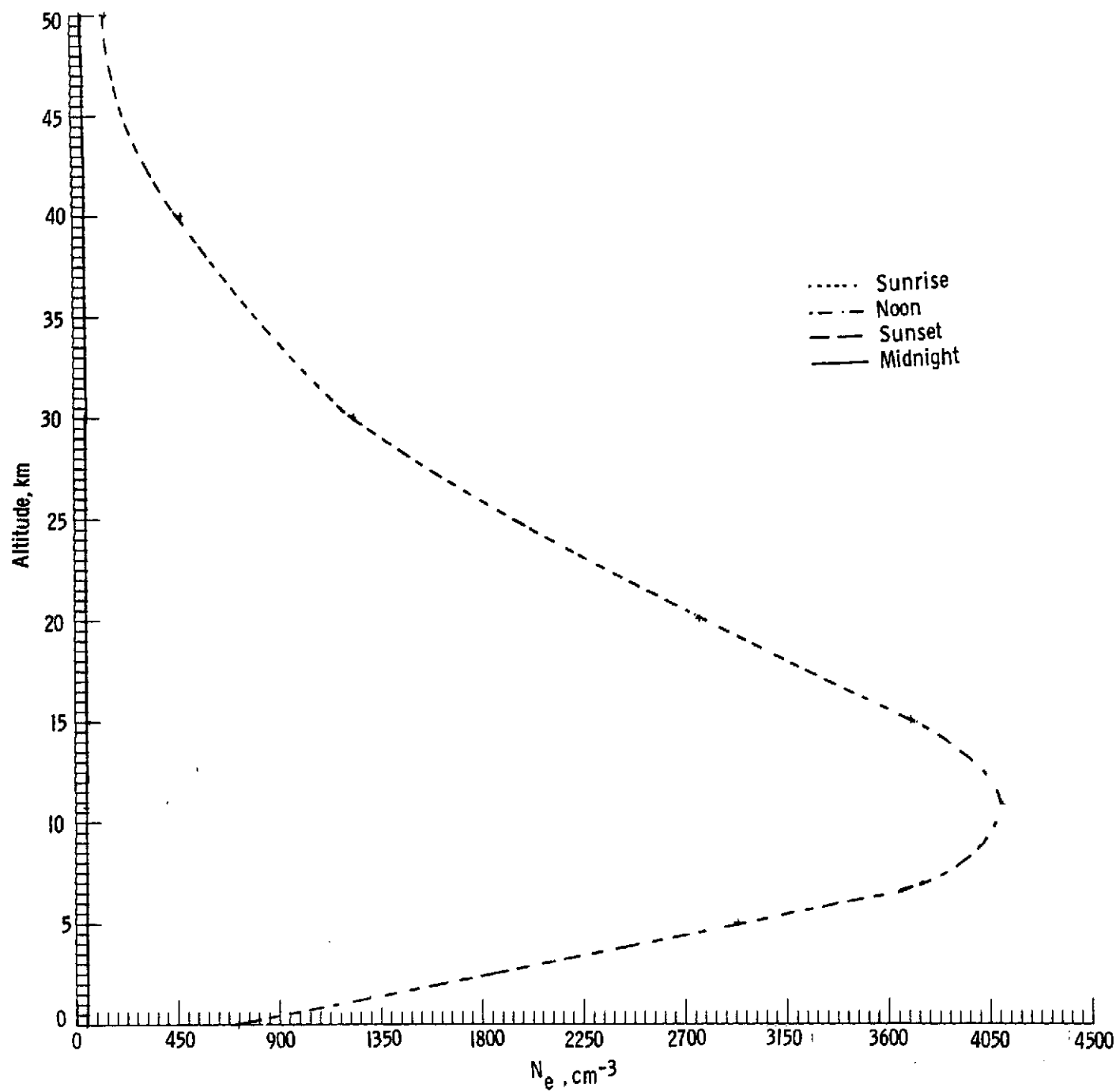
Figure 9b. Electron profile for Model 3.
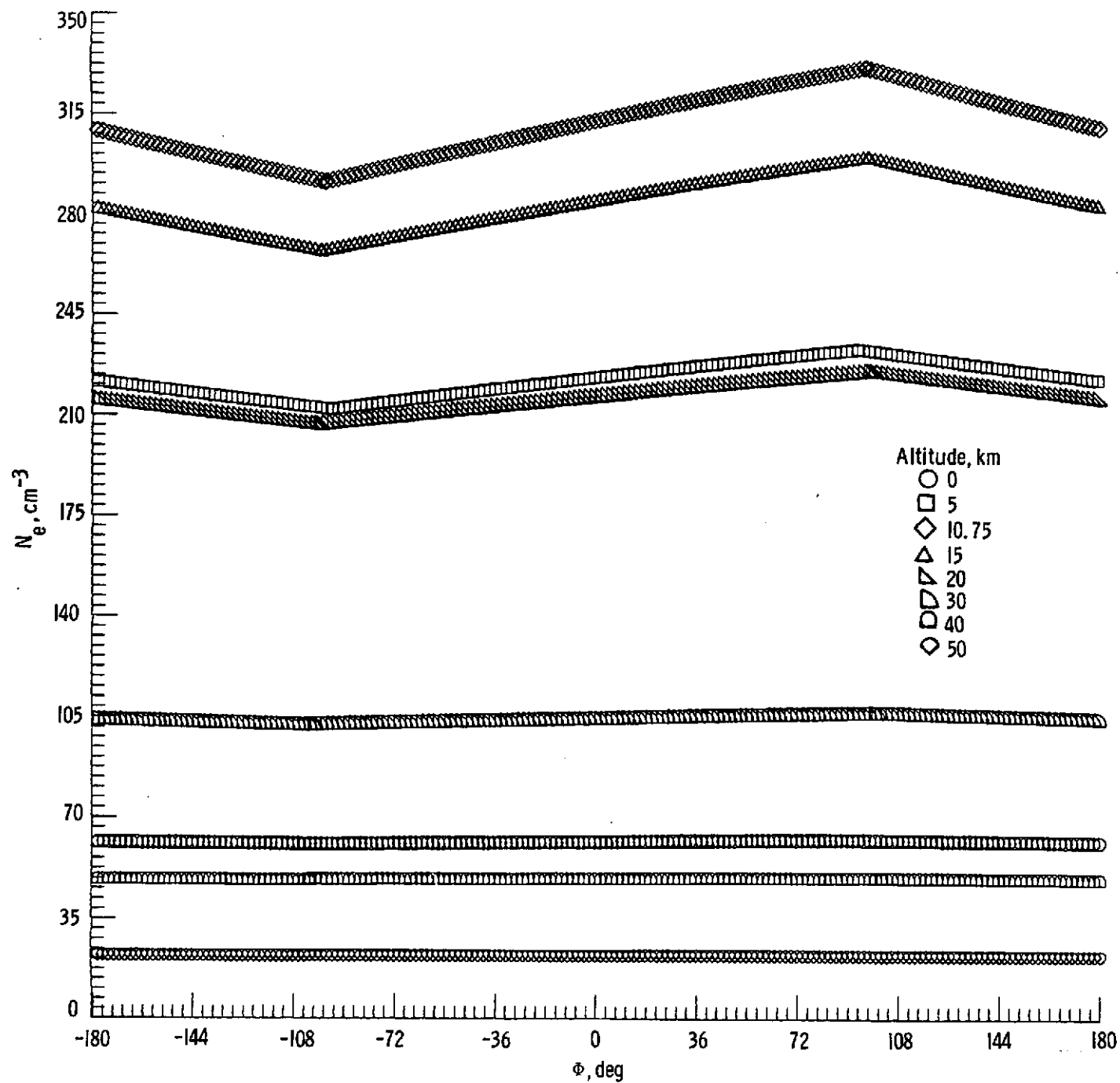
Figure 10a. Electron densities of Model 6 as a function of hour angle.

Figure l0b. Electron profile for Model 6.

Figure IIa. Electron densities of Model 7 as a function of hour angle.
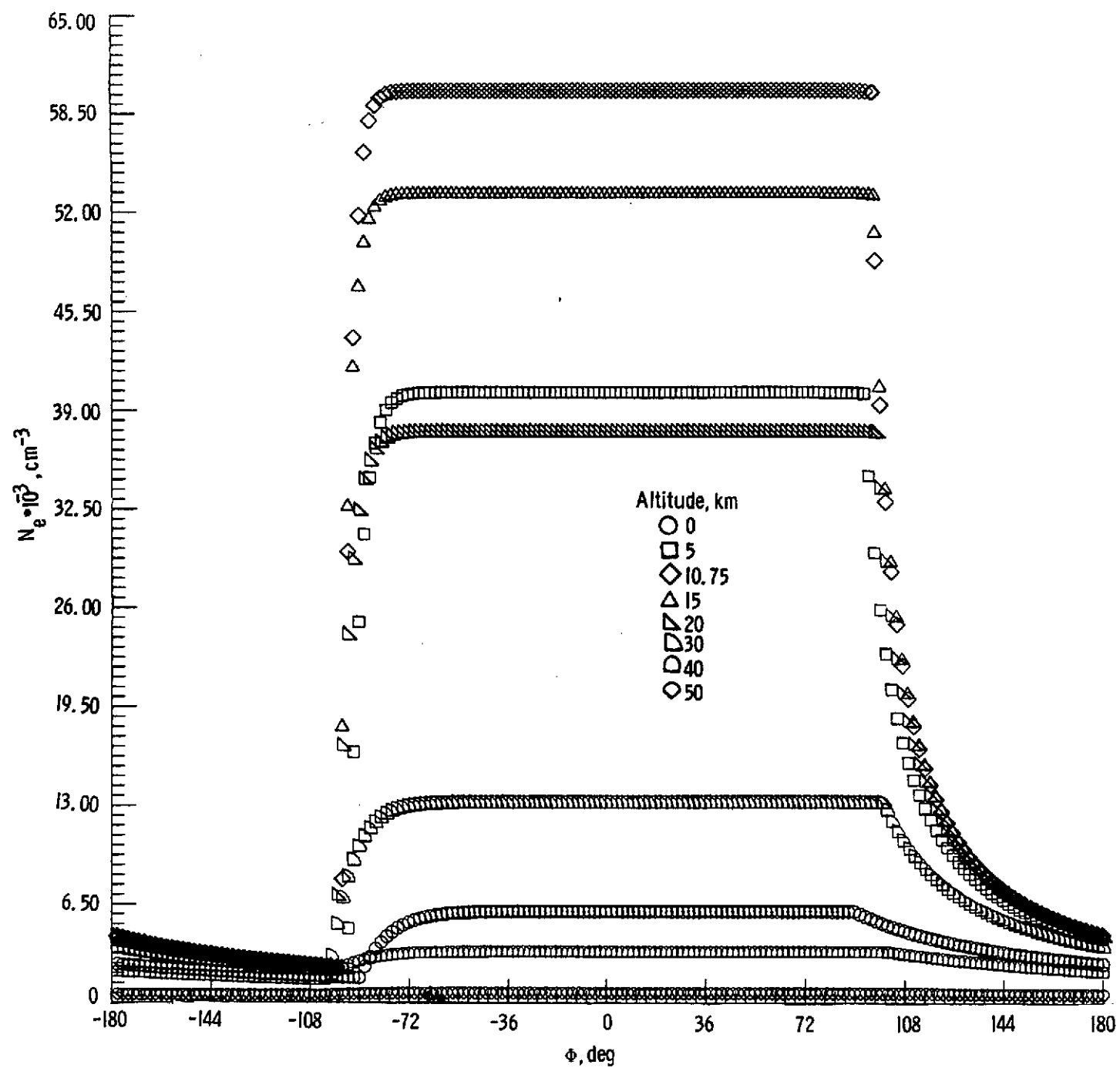
Figure IIb. Electron profile for Model 7.

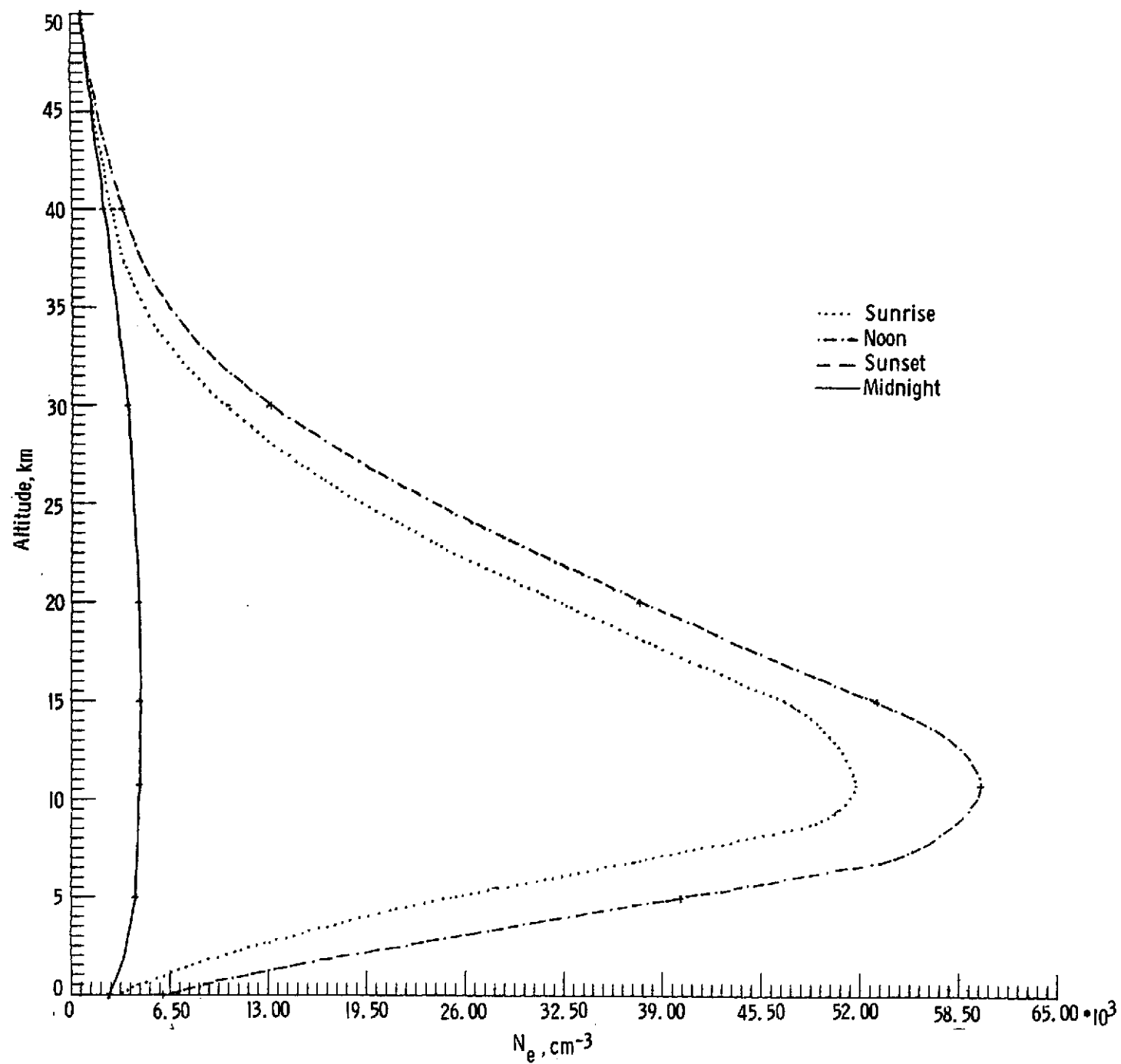Figure I2a Electron densities of Model 8 as a function of hour angle.

Figure l2b. Electron profile for Model 8.